Development of SiO2/rGO from Rice Husk for Photocatalysis, Antioxidant, Electrochemical and green sensor detection Studies

N Swetha
AMC Engineering College
V Venkata Lakshmi
AMC Engineering College
M Mylarappa
mylu4mkallihatti@gmail.com

SJR College for Women
S Chandruvasan
K S Harisha
Bangalore University

Research Article

Keywords: SiO2/rGO, Dye degradation, Antioxidant, Cyclic voltammetry, Sensor

Posted Date: December 19th, 2023

DOI: https://doi.org/10.21203/rs.3.rs-3764801/v1

Additional Declarations: No competing interests reported.

Version of Record: A version of this preprint was published at Silicon on April 12th, 2024. See the published version at https://doi.org/10.1007/s12633-024-02938-5.

Development of SiO_2/rGO from Rice Husk for Photocatalysis, Antioxidant, Electrochemical and green sensor detection Studies

Swetha N[1], Venkata Lakshmi V[1*], Mylarappa M[2*], Chandruvasan S[2], Harisha K. S[3]

[1]Department of Chemistry, AMC Engineering College, Bengaluru, Karnataka, India-560083.
(Affiliated to Visvesvaraya Technological University)
[2]Department of Chemistry, SJR College for Women, Bengaluru, India-560009.
[3]Department of Physics, Bangalore University, Bengaluru-560056, Karnataka, India.

Corresponding authors: mylu4mkallihatti@gmail.com , laxmimurthy@rediffmail.com

Abstract

This study reports the extraction, characterization and development of reduced graphene oxide (rGO) doped silicon dioxide (SiO_2) nanocomposite by simple reflux method. The nanocomposite was confirmed by using X-ray diffraction (XRD), Fourier-transform infrared spectroscopy (FTIR), scanning electron microscopy (SEM) and UV-Visible spectroscopy techniques. The photocatalysis of malachite green (MG) was carried out for rGO, SiO_2 and SiO_2/rGO nanocomposite shows higher MG degradation about 97% compared to rGO, SiO_2 and follows 1st order kinetics. The antioxidant action of SiO_2/rGO nanocomposite was assessed using DPPH shows a more antioxidant activity (98 %) and lower IC_{50} about 488.35 mg/mL. From electrochemical, the specific capacitance (Csp) value of SiO_2/rGO (114 F/g) was exhibits higher compared to rGO (75 F/g) and SiO_2 (96 F/g) respectively. The CV and sensor detection of bee pollen and cow urine samples were performed using nickel mesh electrode in 1M KCl in the potential range -1 to 1 V. The SiO_2/rGO was employed to analyze bee pollen and cow urine concentrations and the detection limits were found to be 0.260 mM and 0.413 mM respectively. The prepared electrode plays an important role for improving sensor detection of bee pollen and cow urine samples.

Keywords: SiO_2/rGO, Dye degradation, Antioxidant, Cyclic voltammetry, Sensor.

1. Introduction

Rice husk ash (RHA) is readily available and abundant as it is a byproduct of burning raw rice husks in developing countries [1]. Interestingly, RHA contains a significant silica content, ranging from 80% to 95% by weight, which could render it a valuable asset in the industrial sector. When RHA is obtained without the process of acid leaching, its silica purity is less than 95 %, and its surface area measures 200 m^2/g, which does not meet the established criteria for commercial silica gel [2-4]. After treating 15 grams of rice husk ash with HCl and citric acid, the purity of the resulting product increased significantly from 82.8 % to 99.3 % and 98.6 %, respectively [5]. In an experiment involving silica extraction and acid leaching as a pretreatment, the surface area was enhanced significantly. For HCl leaching, the surface area increased from 116 m^2/g to 218 m^2/g, and for H_2SO_4 leaching, it increased from 208 m^2/g [6]. RHA has found diverse economic applications. It has been employed in the synthesis of carbon compounds [7], utilized as a source of energy generation, and incorporated into the production of cement or concrete [8]. Rice Husk plays a multifaceted role in various applications. It aids in the removal of toxic metals from wastewater, serves as an organic fertilizer, finds applications in biomedicine, and is utilized for adsorption purposes [9-10]. Rice husk holds the potential for the production of high-value silicon-based compounds like zeolite, silicon carbide, silicon nitride, silicon tetrachloride, and silicates, primarily because of its elevated silica content [11]. Graphene is a two-dimensional material composed of a single layer of carbon atoms arranged in a two-dimensional sp^2 network. Its remarkable physicochemical properties have positioned it as a promising candidate for a wide range of applications [12-13]. Graphene and its derivatives have found applications in a multitude of fields, including nano electronic devices [14], transparent conductors [15], transistors [16], energy-storage capacitors [17], biosensors [18], dye-sensitized solar cells [19], photothermal treatment [20], and drug delivery systems [21].

Silicon-based materials are considered a primary choice for anodes in lithium-ion rechargeable batteries (LIBs) because of their distinctive characteristics. These properties include an exceptionally high theoretical capacity of 4200 mAh g^{-1} with Li_2Si_5 and a low and stable plateau operation voltage of 0.4 V, in contrast to Li/Li^+ [22-24]. SiO_2 is of great interest to scientists due to its anticipated specific capacity of 1961 $mAhg^{-1}$ and its low discharge potential, as reported in studies [25]. During the process of lithiation, an inert matrix composed of lithium oxide (Li_2O) and lithium silicates (Li_4SiO_4) is formed, which can effectively withstand volume changes, as observed in research [26]. However, research revealed that commercial SiO_2 nanoparticles exhibited interactions with lithium ions within a specific voltage range. The reason for this is that reduced graphene oxide (rGO) can coat SiO_2 and form a 3D network architecture, and it can be produced in large quantities, potentially offering advantages in terms of electrode design and mass production [27-28]. In a study by Kasinath Ojha et al., it was reported that graphene-like activated and non-activated porous carbon derived from biomass demonstrated a specific capacitance of approximately 476 F/g when subjected to a current density of 0.2 A/g. This specific capacitance value was notably higher than that achieved with graphene oxide (GO). The electrochemical investigations of these carbon materials reaffirm their potential and promising attributes for use in supercapacitor applications [29-31]. The combination of SiO_2 nanoparticles (NPs) decorating graphene nanoplatelets (GNPs) offers several hybrid characteristics, including improved interfacial contact leading to increased surface area, the establishment of conductive pathways, and the reduction of charge recombination. Graphene/SiO_2 nanocomposites present a more efficient pathway for enhancing photocatalytic performance compared to other carbon-based nanocomposites or SiO_2 alone, primarily due to their incorporation of these distinctive properties [30]. Medications can be linked to graphene through either covalent bonding or non-covalent

interactions, facilitated by the synergistic assembly of SiO_2 and graphene. As a result of these properties, it can serve as a highly efficient nano-carrier for delivering medication to cancer-affected areas [32]. SiO_2 nanoparticles, when used in isolation, lack the capability to achieve this outcome. The aforementioned advantages imply that graphene/SiO_2 nanocomposites have the potential to address the increasing health and environmental challenges associated with water contamination [33].

Silica is commonly used as a flow aid in the production of nutraceutical and medicinal products due to its biochemical inertness [34]. Hybrid nanomaterials that integrate nano-sized SiO_2 particles with specific functions, such as anti-oxidative properties, hold the promise of synergizing the most advantageous characteristics of both components. In contrast to organic polymer matrices, solid inorganic particles like SiO_2 offer numerous advantages, notably enhanced thermal stability and chemical inertness [35]. A novel approach to harness the full advantages of natural antioxidants involves immobilizing them on nanoparticles, creating what are known as "Nano antioxidants." Antioxidant-functionalized SiO_2 nanoparticles are investigated for their radical scavenging capacity (RSC), and the concept of a "nano-antioxidant" is introduced [36-38]. This involves the covalent attachment of Gallic acid, a naturally occurring antioxidant, onto the surfaces of commercially available and well-characterized SiO_2 nanoparticles with sizes ranging from 8 to 30 nm [39-40]. In the current work, rGO doped SiO_2 NCs is developed from raw rice husk and focused on various studies such as photocatalytic, antioxidant, electrochemical and sensors. The nanocomposite was prepared utilizing simple reflux approach and characterized by spectroscopic methods such as XRD, FT-IR, SEM and UV-Visible spectroscopy.

2. Experimental

2.1 Materials and methods

Sodium nitrate ($NaNO_3$) (99 %), Sulphuric acid (H_2SO_4) (99 %), Hydrogen peroxide (H_2O_2) (99 %), Potassium permanganate ($KMnO_4$) (99 %), Tri-Sodium citrate ($Na_3C_6H_5O_7$) (99 %), Sodium sulphite (Na_2SO_3) (99 %), Ammonia (NH_4) (99 %), Ethyl alcohol (CH_3CH_2OH) (99 %), Ascorbic acid ($C_6H_8O_6$) (99 %), Hydrochloric acid (HCl) (99 %), and Graphene powder (GO) were purchased from the Merck Bengaluru are analytical grade was used in the experiment without any modification.

2.2 Collection of rice husk

Raw rice husks were collected from the Chamarajanagar District in the Mysore division of Karnataka state, India (located at 11.9261° N, 76.9437° E). The type of rice husk utilized in the current experiment was 'Sonamasuri' owing to its diverse attributes, including high protein and fiber content, a soft and chewy texture. This rice variety, scientifically known as Oryza sativa L., is typically cultivated over a period of 18 to 24 months, primarily during the summer season.

2.3 Extraction of SiO_2 from raw rice husk

A 50 g sample of Sonamasuri RRH was treated with 2 M HCl solution in 500 mL beaker and dried for 2 hours at 900 °C in a hot air oven with temperature control. The resulting prepared sample was washed continuously with double distilled water until the pH reached 7 and then separated from the solution by filtration. The RRH was further dried for 12 hours at 105 °C and then calcined for 4 hours at 550 °C in a muffle furnace. This process produced approximately 11 g of white RRH ash (WRHA) after combustion. Following that, the white rice husk ash (WRHA) was mixed with 100 ml of 2 M NaOH at 90 °C while being vigorously stirred for 2 hrs., on a magnetic stirrer. This

process was aimed at extracting solid SiO_2 into a water-soluble silicate through a chemical reaction, which is shown in eq. (1).

$$\mathbf{2NaOH + SiO_2 \rightarrow Na_2\,SiO_3 + \ H_2O} \qquad (\mathbf{1})$$

The sodium silicate solution was filtered with filter paper to remove insoluble residues. After filtration, the soluble sodium silicate solution is converted into insoluble silica gel by the reaction with 2 M ascorbic acid (10 ml). Washed orange color silica gel with ethanol to remove by products. Then dried the gel in hot air oven for 600 ℃ for 4 hrs. During this process, the mass of SiO_2 obtained was 2.95 g shown in the Fig. (S1a)

2.4 Synthesis of reduced graphene oxide (rGO)

The stoichiometric weight (1 g) of GO powder was added to a 1 liter beaker placed in an ice bath, maintaining temperature range between 0 °C to 6 °C. This was achieved by initially adding 1g of $NaNO_3$ and by the gradual addition of H_2SO_4 into the reaction mixture with continuous stirring using REMI magnetic stirrer. Subsequent, 6 g of $KMnO_4$ was introduced over a period of 3 hours, with continuous stirring to prevent any spillage or effervescence of the mixture. After 2 hours, the beaker was taken out of the ice bath and transferred to magnetic stirrer with hot plate. The temperature was kept at 30 °C initially and gradually increased every half hour until the color of the mixture turned to a brownish-black. While stirring continuously, 100 mL of water was introduced and the heat source was turned off after 2 hours. Subsequently, 80 ml of H_2O_2 was added to halt the reaction and eliminate excess $KMnO_4$, leading to the formation of a yellow-colored solution once the precipitate solution slowly settled. The resultant precipitate solution was filtered through a funnel and then subjected to 24 hrs heating in a hot air oven, with the temperature being kept below 90 °C [26].

2.5 Synthesis of SiO_2/rGO NPs

The prepared rGO about 0.6 g was dispersed in 50 mL of water and thoroughly mixed. Then, 0.2 g of SiO_2 was added to the mixture and stirred using a magnetic stirrer for about 60 minutes. After 1 hour stirring, 1 % sodium citrate was boiled for 55 minutes and 0.1 mg of sodium sulphite in 5 ml of distilled water was added to the above mixture and stirred at 100 °C for 3 hrs. The solution was cooled, filtered and washed with distilled water and ethanol. Finally, the prepared nanocomposite was dried in an oven at 100 °C for about 1 hr. The schematic diagram of SiO_2/rGO preparation was shown in the Fig. (S1b).

2. Results and discussion

2.1. X-ray Diffraction studies (XRD)

The XRD measurements of RRH, SiO_2, rGO, and SiO_2/rGO NCs are shown in Fig. 1. In particular, Fig. 1 (a) illustrates the amorphous characteristics of RRH at an angle of $2\theta=22.34^{o}$, where the Miller planes correspond to (100) [41]. Fig. 1 (b) reveals well-crystalline SiO_2 NPs with sharp peaks, signifying the absence of impurities in the material at 550 ℃. The XRD pattern exhibits peaks corresponding to Miller planes (100), (001), (002), (011), (200), (012), (110), (013), and (020) [52]. In Fig. 1 (c), one can observe that the XRD spectra of rGO exhibit a broader peak at $2\theta=26.10°$. This broadening suggests that the π-conjugated structure of graphene has been notably restored following the removal of oxygen-containing functional groups during the chemical reduction process, as documented in prior research [43-44]. In Fig. 1 (d), the spectrum of SiO_2/rGO demonstrates a significant reduction in the diffraction intensity of the (001) plane, along with the emergence of diffraction peaks corresponding to the (100) and (400) planes in this novel hybrid material. These results suggest that the successful combination of graphene oxide (GO) and nano-SiO_2 took place through electrostatic self-assembly, resulting in the formation of GO-SiO_2 hybrids.

After chemically reducing the GO-SiO_2 hybrids to rGO-SiO_2, the diffraction intensity of the (001) plane is further diminished, and the diffraction peaks associated with the (100) and (400) planes no longer appear [45]. Instead, a new broad peak arises at approximately 2θ=26.5°, which can be attributed to the (002) plane. These results imply that the reduction process resulted in the restacking of the rGO sheets [26]. The average crystallite size can be determined using the Debye-Scherrer equation, as outlined in eq. (2), [46].

$$\boldsymbol{D = \frac{0.9\,\lambda}{\beta\,\mathrm{Cos}\theta}} \qquad (2)$$

Where λ is the X-ray wavelength, β is the full width at half maximum (FWHM) of the diffraction line, and θ is the diffraction angle. The constant k, which is normally about 0.90, is controlled by the grain structure. Table 2 presents the calculated average crystallite sizes for RRH, SiO_2, rGO, and SiO_2/rGO NCs, which were determined to be 50.76, 60.82, 14.98, and 24.48 nm, respectively. The XRD patterns of these samples displayed intense and well-defined peaks, signifying their excellent crystallinity. Notably, no impurity peaks were detected, indicating the high purity of the prepared samples. A strong and narrow peak in the XRD pattern is indicative of well-crystalline particles [47]. To determine the total crystalline sizes of the samples, both Scherrer's equation and the Williamson and Hall approach were analyzed.

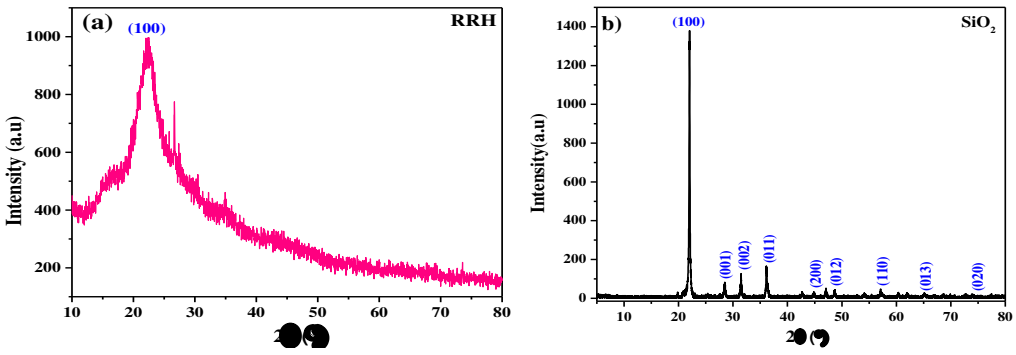

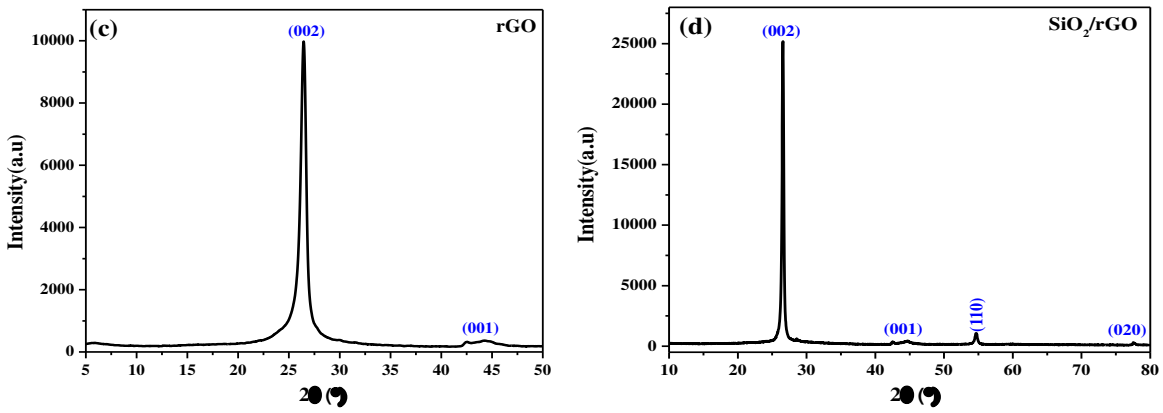

Fig. 1. XRD spectrum of (a) RRH (b) SiO_2 (c) rGO (d) SiO_2/rGO.

The Hall and Williamson method takes into account both the domain effect and lattice micro-strain effect, which collectively contribute to the broadening of lines in the XRD pattern. The combined impact of these factors can be observed in the final full width at half maximum (FWHM), which represents the sum of the grain size and lattice distortion.

$$\mathrm{Cos}\theta = \varepsilon(4\mathrm{Sin}\theta) + \frac{\lambda}{D} \qquad (3)$$

Eq. (3) elucidates a linear correlation between 4sinθ and β cosθ, with ε denoting the strain linked to the nanocomposites. The intercept of the line, which is at 0.90(λ)/D, yields the crystallite size (D), while the slope of the line gives the strain (ε). The values obtained from this equation were found to be in agreement with the crystallite sizes calculated using Scherrer's equation. Various structural parameters, including dislocation density (δ), strain (ε), and stacking fault (SF), were influenced by the underlying relationships and are presented in Table 1.

Table.1. The mean crystallite size of RRH, SiO_2, rGO, and SiO_2/rGO nanocomposite.

Sample	FWHM (rad)x10^{-3}	Size (nm)	W-H Plot (nm)	Strain (ε)×10^{-3}	Stacking fault (SF)	Dislocation density (δ) x10^{-3}
RRH	4.579	80.76	81.23	0.997	0.678	1.26
SiO_2	3.514	60.82	59.44	0.556	0.574	0.27
rGO	31.067	14.32	15.65	8.655	0.236	12.40
SiO_2/rGO	5.883	26.48	25.79	2.036	0.520	1.42

2.2. Fourier Transform Infrared Spectroscopy (FT-IR)

Fig. 2 presents the FT-IR spectrum of Raw Rice Husk, SiO_2, rGO, and SiO_2/rGO NPs. In Fig. 2 (a), the FT-IR spectra of RRH exhibit various peaks at different frequencies, including 3404.3 cm^{-1} for O-H groups, 2925.8 cm^{-1} for C-H groups, 1641.3 to1737.7 cm^{-1} for C=O groups, 1546.8 to 1652.9 cm^{-1} for C=C groups, 1461.9 cm^{-1} for CH_2 and CH_3 groups, 1380 cm^{-1} for CH_3 groups, 1379.0 cm^{-1} for aromatic CH stretching and carboxyl-carbonate structures, 1153.4 to 1300 cm^{-1} for C=O groups, 1238 cm^{-1} for CH-OH groups, 1080 cm^{-1} for Si-O-Si groups, and 862.1-476.4 cm^{-1} for Si-H groups [48-50]. In Fig. 2 (b), the FT-IR spectra of silica extracted from RRH reveal four prominent peaks. The broad peak, centered at 3400 cm^{-1}, is attributed to the O-H stretching of the hydroxyl group [51]. The peak observed at 1100 cm^{-1} corresponds to the asymmetric stretching vibration of the Si-O-Si group [52]. Furthermore, the peak at 460 cm^{-1} is associated with the O-Si-O bending vibrational mode, and the peak at 800 cm^{-1} corresponds to the symmetric stretching of the Si-O-Si group [53]. In Fig. 2 (c), the FT-IR spectra reveal the deformation of water molecules at 1630 cm^{-1} and alkoxy C-O stretching vibrational modes at around 1043 cm^{-1}. Furthermore, the peaks at 1448 cm^{-1} are associated with =CH in-plane vibrations, and those at 780 cm^{-1} correspond to -CH out-of-plane vibrations. The broad peak observed at 3400 cm^{-1} can be attributed to the vibrations of adsorbed water molecules or skeletal vibrations corresponding to unoxidized graphitic domains [54-57]. Significantly, the spectra do not exhibit peaks typically associated with C-OH (~1340 cm^{-1}), C = C (~1570 cm^{-1}), and -COOH (~1710-1720 cm^{-1}) groups. The absence of C = C bonds indicates strong oxidation. Consequently, this spectrum differs markedly from the spectra of reduced graphene oxide or chemically derived graphene [58]. In Fig. 2 (d), the FT-IR spectrum exhibits a prominent peak at 1101 cm^{-1}, attributed to the stretching vibrations of Si-O-C or Si-O-Si bonds, and a peak at 968 cm^{-1}, corresponding to the bending

vibrations of Si-OH bonds [59]. The stretching and bending vibrations of Si-O bonds are detected at 796 cm^{-1} and 471 cm^{-1}, respectively, confirming the presence of SiO_2 nanoparticles in the nanocomposites produced in this study. The faint or indistinct spectra of rGO in Fig. 2 (d) can be attributed not only to the incomplete reduction of GO but also to the interaction between oxygen functional groups and Si-OH. The formation of a covalent bond, Si-O-C, between rGO sheets and SiO_2 nanoparticles indirectly confirms this reaction [60]. These results suggest that the SiO_2 nanoparticles were effectively dispersed on the surface of rGO sheets.

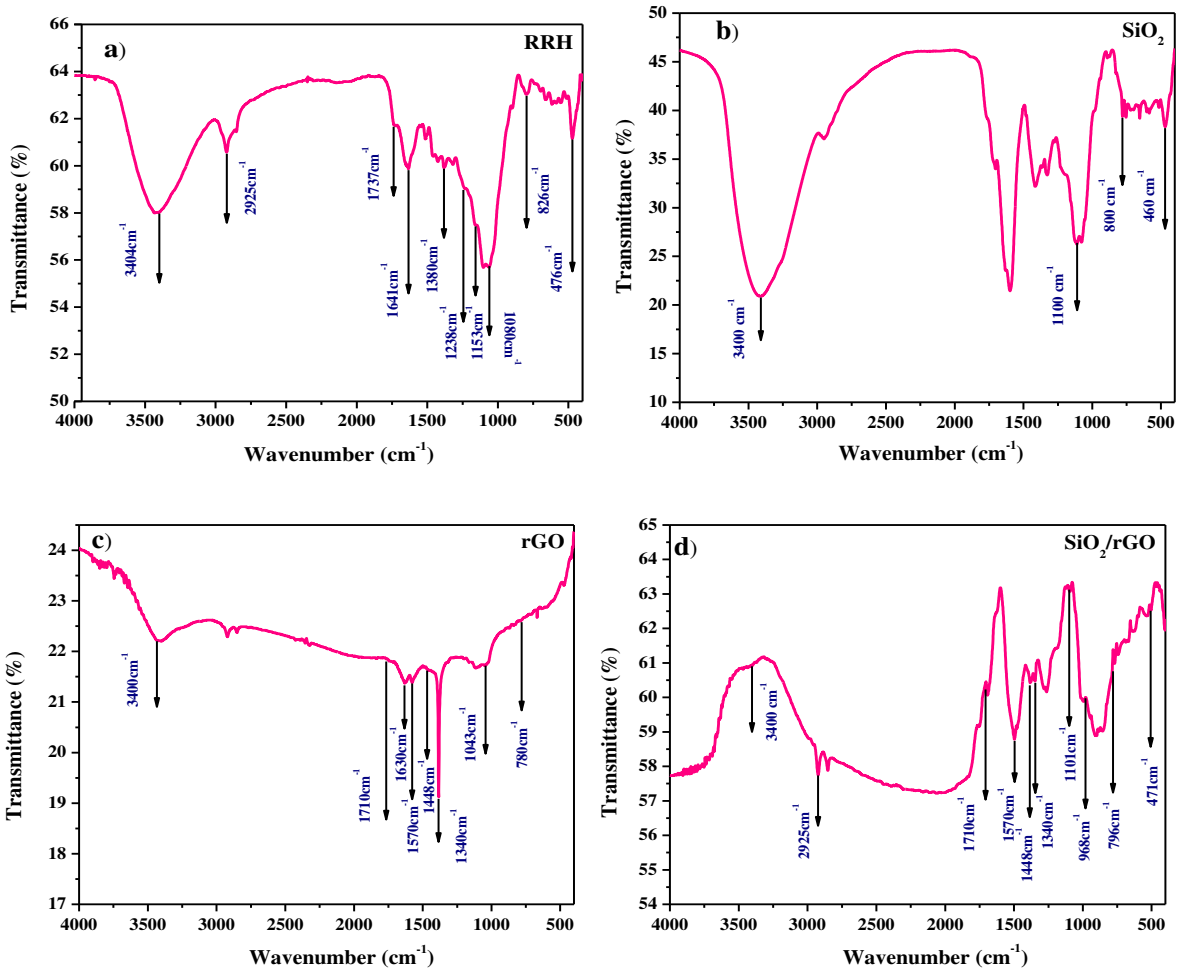

Fig. 2. FT-IR spectrum of (a) RRH (b) SiO_2 (c) rGO (d) SiO_2/rGO.

2.3. Scanning electron microscopy (SEM)

Fig. 3 showcases the SEM images of RRH, SiO_2, rGO, and SiO_2/rGO NPs. In Fig. 3 (a), the image exhibits a resemblance to tree bark or a wooden log, suggesting the amorphous nature of the compound. Furthermore, the particles are unevenly distributed across the area, and there is noticeable surface roughness on the particles [61]. In Fig. 3 (b), the particles are closely packed, forming an agglomeration that is evenly spread across the surface, creating small globular shapes with a prominent pore in the region [62]. In Fig. 3 (c), the image depicts reduced graphene, and it is clear that the graphene sheets are dispersed across the area, and evenly spread throughout the graphene layer. Moreover, certain regions seem to show sheets that are crushed or layered on top of each other, resembling a bundle of graphene layers stacked together [63]. In Fig. 3 (d), the image reveals the prepared nanocomposite SiO_2/rGO. Small silica spherical structures are dispersed unevenly within the graphene layer and there is evidence of the graphene layer breaking down into individual sheets, likely caused by bond breakage resulting from the bonding of silica nanoparticles with rGO through the reflux method [64].

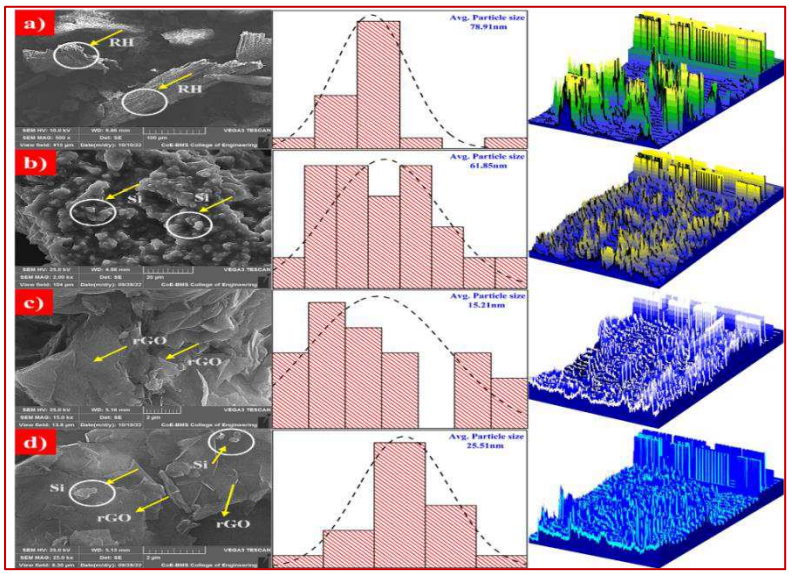

Fig. 3. SEM, Size analyzer and 3D surface plot of (a) RRH (b) SiO_2 (c) rGO (d) SiO_2/rGO.

2.4. UV-Visible Spectroscopy

The UV-visible spectroscopy is a one of the most powerful tools is used to characterize the prepared samples of RRH, SiO_2, rGO, and SiO_2/rGO nanocomposite. Fig. S2 displays the absorbance v/s wavelength pattern of RRH, SiO_2, rGO, and SiO_2/rGO NCs. The energy band gap can be found using the Kulbeka Munk function, which also provides the absorption spectra, as shown by equation (3) and the Kulbeka Munk is modified into the Tauc relation in eq. (4).

$$\mathbf{F(R) = \frac{1 - R^2}{2R}} \qquad (3)$$

$$\mathbf{(F(R)h\nu)^2 = C(h\nu - Eg)} \qquad (4)$$

Where, Eg is stand for energy band gap, C is constant and the energy of a photon is hυ. $(F(R)h\upsilon)^2$ is obtained using eq. (4). The optical band gap is deliberate by plotting (hυ) v/s $(F(R)h\upsilon)^2$, after that, at the inflection point, forming a tangent towards $(F(R)h\upsilon)^2 = 0$. As can be noticed in Fig. S2 (a), (b), and (c), the band gaps of RRH, SiO_2, rGO, and SiO_2/rGO NCs were determined to be 3.90, 2.42, 4.54, and 1.64 eV, respectively [70, 71].

2.5. Photocatalysis studies

Photocatalytic studies of MG dye, rGO, SiO_2, and SiO_2/rGO were carried out in a standard 250 mL beaker with a surface area of 100 square millimeters. A Philips UV lamp, which emitted 115 watts of power, was used as the source of illumination. The UV-Vis spectrometer scanned wavelengths spanning from 200 to 900 nm, and the choice of 618 nm, which exhibited the highest intensity within the UV spectrum, was made from the range of 400 to 720 nm. This selection was made without the implementation of any filters. Under regular atmospheric conditions, the light was directly applied to the reaction mixture from a distance of 15 cm. All experiments were carried out with double-distilled water. In the established protocol, the process entailed dissolving 10 mg of rGO/SiO_2 photocatalyst in 150 mL of a 20 ppm dye solution. The mixture was consistently

stirred at 400 rpm using a magnetic stirrer [72-73]. Fig. 4 depicts the UV absorption spectrum of MG dye decomposition for MG, rGO, SiO_2, and SiO_2/rGO. At specified time intervals, 4 mL sample of the reaction mixture was extracted from the chemical dye solution. The photocatalytic assessment of dye, rGO, SiO_2, and SiO_2/rGO nanocomposites involved the discoloration of an industrial dye under UV light exposure, with measurements taken at consistent 10 minute intervals. MG dye was selected as a representative water pollutant due to its environmentally harmful properties. It exhibited a prominent absorption peak at 546 nm, as illustrated in Fig. 4 (a, b, c, d). During the initial phases of photocatalytic experiments, tests were conducted in the absence of light, and during this period, the dye exhibited minimal degradation. Nevertheless, when subjected to 150 minutes of UV light exposure, the degradation percentages were as follows: 36.73 % for MG dye, 57.82 % for rGO, 77.70 % for SiO_2, and 96.59 % for rGO/SiO_2, as demonstrated in Fig. 4 (a, b, c, d). In response to UV light exposure, these measurements were recorded at consistent 10 minute intervals as depicted in Fig. 4 (a). The efficiency of photocatalytic discoloration for MG dye was calculated using eq. (4) [74].

$$\% \, D = \frac{C_0 - C}{C_0} \times 100 \qquad (4)$$

Where, D is the degradation, C_0 and C are the final and initial concentration of the sample. Drawing from the observed photocatalytic efficiency of the catalysts, an attempt has been made to propose a potential degradation mechanism. In an ideal scenario, when a nanomaterial is exposed to incident photons with energy equal to or exceeding the band gap, it leads to the separation of charges.

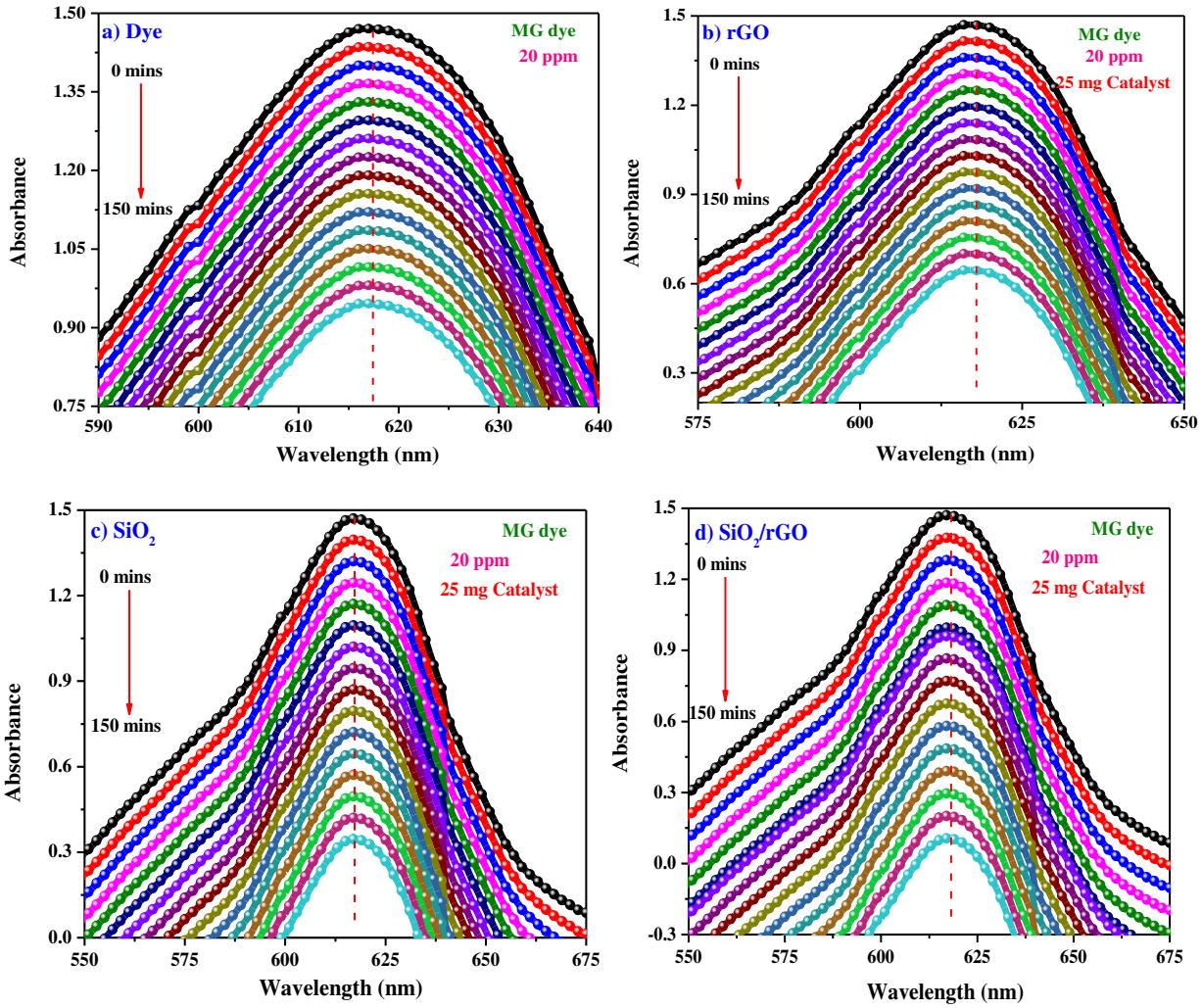

Fig. 4. UV absorption spectrum of (a) MG dye (b) rGO (c) SiO_2 (d) SiO_2/rGO.

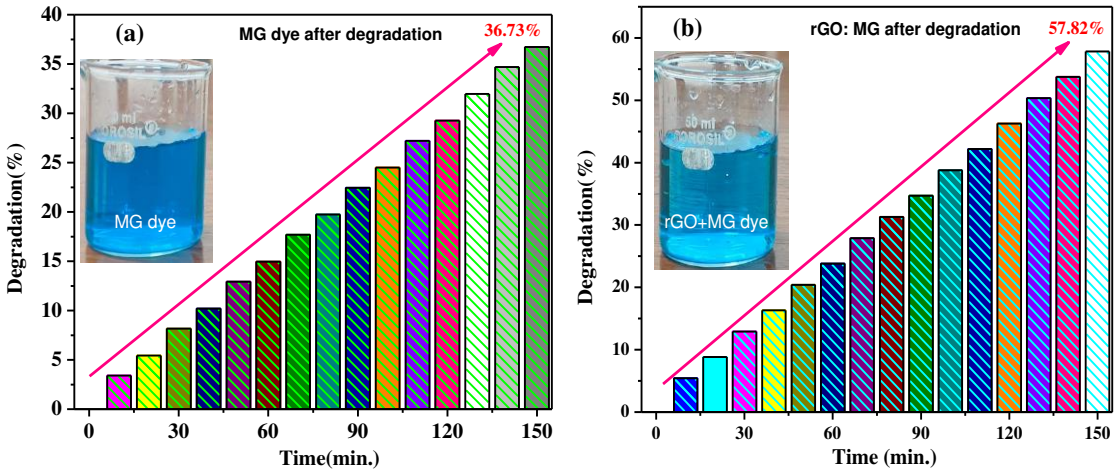

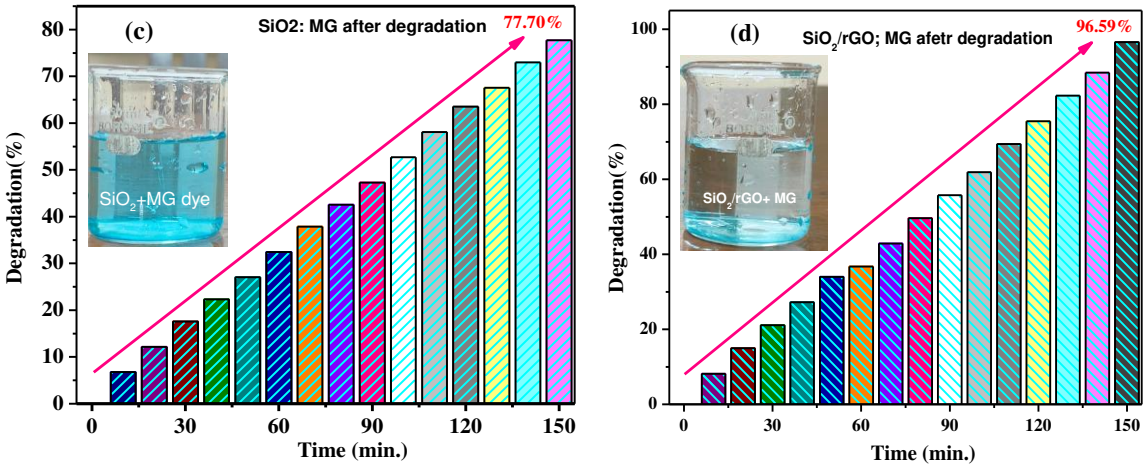

Fig. 5. Percentage degradation of MG dye (a) MG dye (b) rGO (c) SiO_2 (d) SiO_2/rGO.

Consequently, the holes generated in the valence band facilitate the oxidation of the adsorbed dye, resulting in the generation of hydroxyl radicals. Furthermore, the kinetics study, derived from the graph of $-\ln(C/C_0)$ versus time, demonstrates a gradual degradation as time progresses, as illustrated in Fig. 5 (a, b). This observation suggests the presence of a first order degradation mechanism, as indicated in eq. (5) [75],

$$-\ln\left(\frac{C}{C_0}\right) = -Kt \qquad (5)$$

Where C_0, C, t and k are initial dye concentration, dye concentration at t (min), decolourisation time (min) and decolourisation rate constant (1/min), respectively.

Moreover, the degradation half-life ($t_{1/2}$) representing the time needed for 50 % of the dye to degrade was computed as follows: 69.65 minutes for MG, 76.49 minutes for rGO, 74.83 minutes for SiO_2 and 79.96 minutes for SiO_2/rGO were depicted in Fig. 7 (a, b, c, d). The recorded half-life values emphasize the significant impact of the composite in accelerating the degradation of MG dye, primarily due to the presence of rGO. This notably indicates that the photocatalytic efficiency of SiO_2/rGO betters that of MG dye, rGO, and SiO_2. This trend becomes more

pronounced when considering the k values, as the reaction rate of the nanocomposite is approximately 79.75 % greater than that of the SiO_2.

The degradation provides compelling evidence for the advantages of rGO in improving photocatalytic efficiency. We are certain that the exceptional photocatalytic performance was achieved through the remarkable hybrid structure formed between SiO_2 and rGO, combined with the high conductivity of the latter. At the same time, the electrons produced in the conduction band engage in a reaction with surface oxygen, resulting in the formation of reactive oxygen species. Ensuring the prevention of recombination between the generated electrons and holes is crucial for achieving effective photocatalysis [76-78].

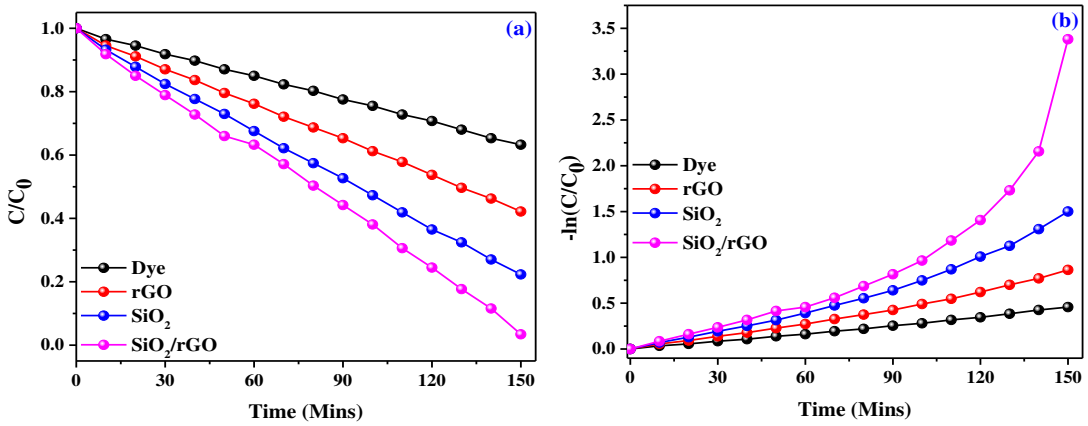

Fig. 6. Plot of (a) C/C_0 and (b) $-\ln(C/C_0)$ for decolonization of MG of the prepared sample.

Furthermore, a significant increase in the concentration of hydroxyl ions on the catalyst surface indicates improved photocatalytic activity. During the current study, a similar trend was observed in the photocatalytic assessments of MG dye, rGO, and SiO_2. Nonetheless, a noticeable enhancement in photocatalytic performance was apparent in the case of SiO_2/rGO. This phenomenon can primarily be attributed to the presence of the 2D π-conjugation system within rGO, which promotes the efficient movement of electrons towards the conduction band. The migration of electrons plays a crucial role in propelling the degradation reaction, leading to the

formation of superoxide radicals which, in turn, give rise to hydroxyl radicals. This sequence effectively lowers the chances of recombination with holes [79]. The comprehensive results collectively affirm that both SiO_2 and combination of SiO_2 with rGO exhibit exceptional photocatalytic capabilities in the decolourisation of MG dye. This underscores a notably increased effectiveness in photo decolourisation. The incorporation of rGO into SiO_2 contributes to the improvement of free electron and hole production [80]. This improvement becomes evident when exposed to visible light energy ($h\upsilon$) that matches or exceeds the energy of the material's band gap ($h\upsilon \geq Eg$). In such circumstances, the irradiation initiates the formation of positively charged holes (h^+) in the conduction band (CB) aided by the transfer of electrons (e^-) from the valence band (VB) [81]. Photo-generated electrons stemming from both SiO_2 and the fusion of SiO_2 with rGO display a seamless migration toward the material's surface. This movement facilitates the generation of anion radicals (O_2^-) from molecular oxygen. At the same time, photo-generated holes situated on the valence band (VB) of SiO_2 and SiO_2 when combined with rGO can directly oxidize the dye or produce hydroxyl radicals (OH) from water molecules adsorbed on the surface [75].

In the photocatalytic procedure, the active radicals include OH^*, O_2^{*-} and the photo-generated holes. These active species play a vital part in the oxidation of adsorbed dye molecules, where the highly reactive O_2^- and OH actively propel the oxidation process. In the case of SiO_2, the valence band primarily originates from Si (3d) states, while the conduction band is linked to O (1s) states. The degradation mechanism can be attributed to the interaction between dye molecules and hydroxyl radicals, which are generated through ultrasonic irradiation in the presence of SiO_2/rGO nanocomposites [82-84]. SiO_2 nanoparticles exhibited photoexcitation, which was linked to charge transfer from the Si-O bonding orbital to the 2p nonbonding orbital of non-bridging oxygen. When a UV photon interacts with the SiO_2 surface, it causes an electron in the

valence band (VB) to transition to the conduction band (CB), creating a positively charged hole (h^{+}_{VB}) in the process. The negative charge becomes intensified within the conduction band (e^{-}_{CB}), leading to the formation of photocatalytic active centers on the SiO_2 nanoparticle's surface shown in eq. (6).

$$SiO_2 + hv \rightarrow e^{-}_{cb} + h^{+}_{vb} \qquad (6)$$

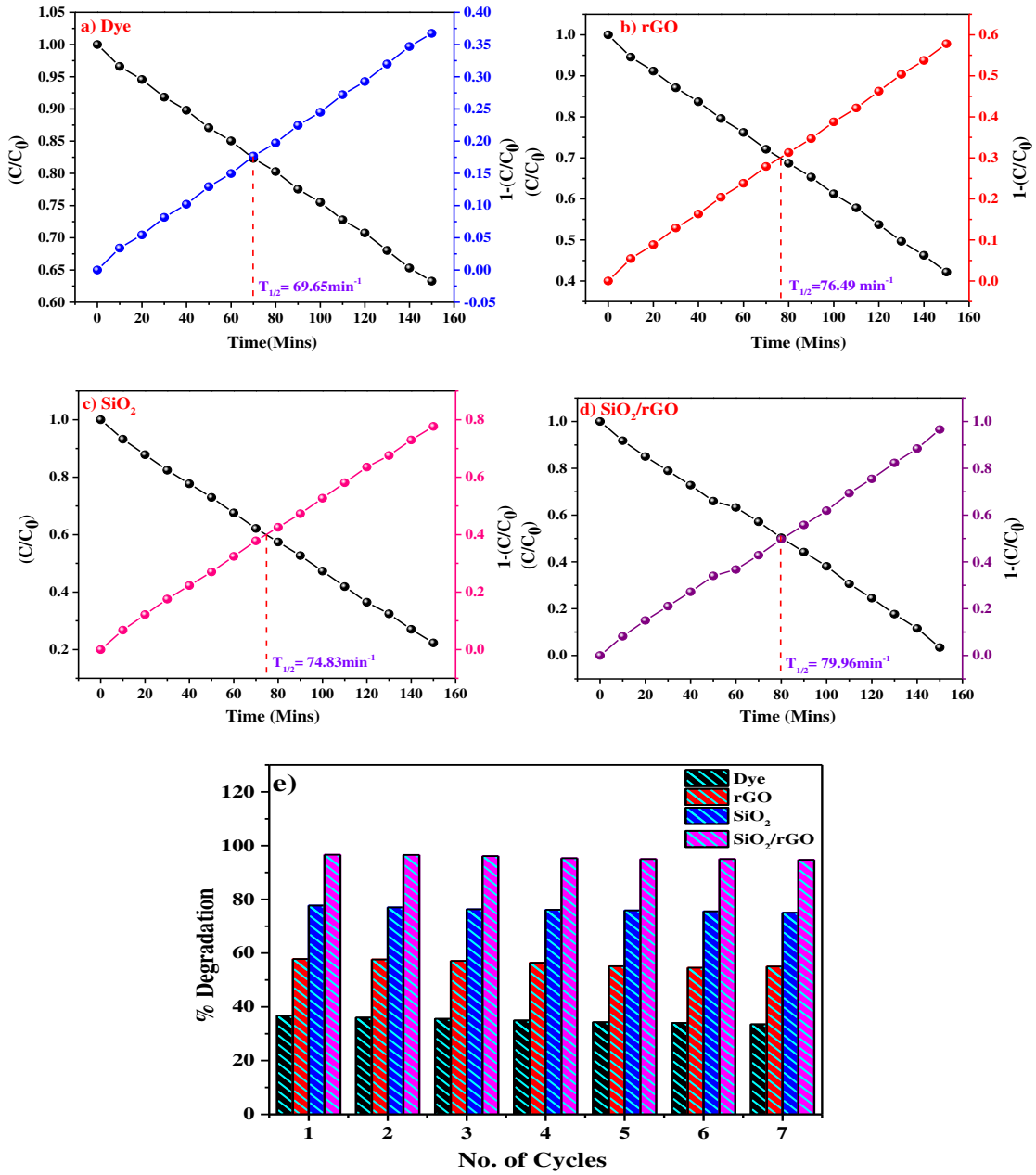

Fig. 7. Half-life time of (a) MG (b), rGO (c) SiO_2, (d) SiO_2/rGO (e) Reusability of the catalyst.

The holes in the valence band react with chemisorbed H_2O molecules, resulting in the generation of reactive species like $^{\bullet}OH$ radicals. These $^{\bullet}OH$ radicals then go on to react with dye molecules, leading to their complete degradation. The primary function of the surface particles deposited is to absorb electrons and transfer these electrons either to H^+ ions or to $O_2^{\cdot}$ slowing down the recombination of electron-hole pairs will enhance both the efficiency of photocatalysis and the speed of hydroxyl radical generation, ultimately leading to an increased rate of degradation of MG dye [85-86]. Table 2 shows the photocatalysis activity from the previous study for the comparison studies. The recycling and reuse of the photocatalysts for the photocatalytic oxidation of MG dye solutions was tested. The experiment was conducted under the following parameters: a reaction time of 150 minutes, a concentration of 20 ppm for the MG dye solution, and a quantity of 10 mg in a 150 ml volume for the SiO_2/rGO composite. The results demonstrate consistent photocatalytic performance even after undergoing 7 cycles, indicating the enduring stability of the photocatalyst in the oxidation of MG dye solutions. This suggests the potential for recovering and reusing the photocatalyst without compromising its stability, positioning it as a promising candidate for applications in environmental remediation [87].

In a more detailed explanation, the composite comprises SiO_2 nanoparticles dispersed on the surface of the graphene oxide (GO) sheet. It is highly probable that these nanoparticles are stimulated and initiate the generation of electron-hole pairs (e^-/h^+) when exposed to visible light, as represented in eq. (7). The electron produced through photoexcitation migrates from the conduction band (CB) of the SiO_2 nanoparticles to the surface of the graphene oxide (GO), as described in eq. (8). This movement results in the reduction of oxygen molecules, leading to the formation of superoxide radicals, known as $O_2^{\cdot -}$, as outlined in eq. (9). Additionally, the presence of an electron deficiency (hole) in the valence band (VB) is responsible for generating hydroxyl

radicals ($OH^{\cdot}$), as indicated by eq. (10). The primary reactive species generated during the study of photo-degradation, namely superoxide radicals ($O_2^{\cdot -}$) and hydroxyl radicals ($OH^{\cdot}$), play a pivotal role in breaking down organic pollutants into environmentally benign degradation byproducts, specifically carbon dioxide (CO_2) and water (H_2O) molecules, as illustrated in eq. (11) and (12) [89-90].

$$SiO_2 + hv \rightarrow SiO_2(h^+) + SiO_2(e^-) \quad (7)$$

$$SiO_2(e^-_{CB}) + rGO \rightarrow rGO(e^-) + SiO_2 \quad (8)$$

$$rGO(e^-) + O_2 \rightarrow rGO + O_2^- \quad (9)$$

$$SiO_2(h^+_{VB}) + OH^- \rightarrow SiO_2 + OH \quad (10)$$

$$O_2^- + 2H_2O + e^- \rightarrow 3OH^- + OH^{\cdot} \quad (11)$$

$$O_2^- + OH^{\cdot} + Dye \rightarrow CO_2 + H_2O \quad (12)$$

Table 2. Comparative study of nanocomposites used in previous research on photocatalysis.

Nanomaterial	Dye	Time (min)	Degradation (%)	Reference
SiO_2	Methyl red	120	95	[91]
SiO_2/α-Fe_2O_3	Acid Black 1	120	82.96	[92]
ZnO-CuO/RHA	Methylene Blue	180	99.46	[93]
SiO_2	Methyl Orange	180	95	[94]
SiO_2@TiO_2	Rhodamine B	210	66.82	[95]
ZnO/SiO_2	Methylene Blue	240	89.95	[96]
Zn-TiO_2/C@SiO_2	Rhodamine B	80	95	[97]
Fe doped SnO_2-SiO_2	Methylene Blue	270	74	[98]
Sm/SnO_2 - SiO_2	Methylene Blue	260	78	[99]
Fe_3O_4@SiO_2@AgO	Phenol red	70	89	[100]
SiO_2/rGO	**MG**	**150**	**96.59**	**Present study**

2.6. Antioxidant studies

The DPPH free radical scavenging method was employed to evaluate the antioxidative capabilities of rGO, SiO_2, and SiO_2/rGO. A stock solution was prepared by dissolving 20 mg in 20 mL of water yielding a concentration of 1 mg/ml. Furthermore, 0.004 g of DPPH was dissolved in 100 mL of methanol. After the initial mixing of DPPH and methanol, the resulting solution was administered to samples in varying quantities. Afterward, the absorbance at 517 nm was determined using a UV-Vis spectrophotometer following the incubation of the tubes at 25 °C for 90 mins. To attain a 50 % reduction in free radicals, a specific time duration and expected concentrations for each fraction were necessary. To evaluate the antioxidant effects, divide the solution into five distinct test tubes, allocating different volumes to each tube (100, 200, 300, 400, 500, and 600 µL). The next step includes the addition of methanol into the test tubes using a micropipette to ensure even distribution throughout the tubes. To prevent the evaporation of the DPPH solution, dispense 2 mL of the solution into each test tube and then cover the tubes with aluminum foil. The mixture should be left undisturbed in the dark for about 90 minutes before proceeding with any further analysis using a UV instrument. The calculation of antioxidant activity was conducted for rGO, SiO_2, and SiO_2/rGO nanocomposite [101].

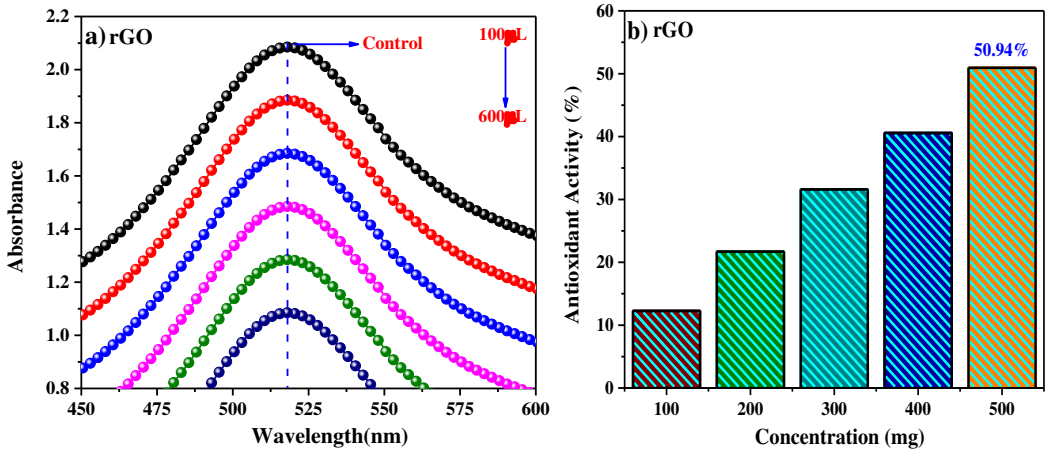

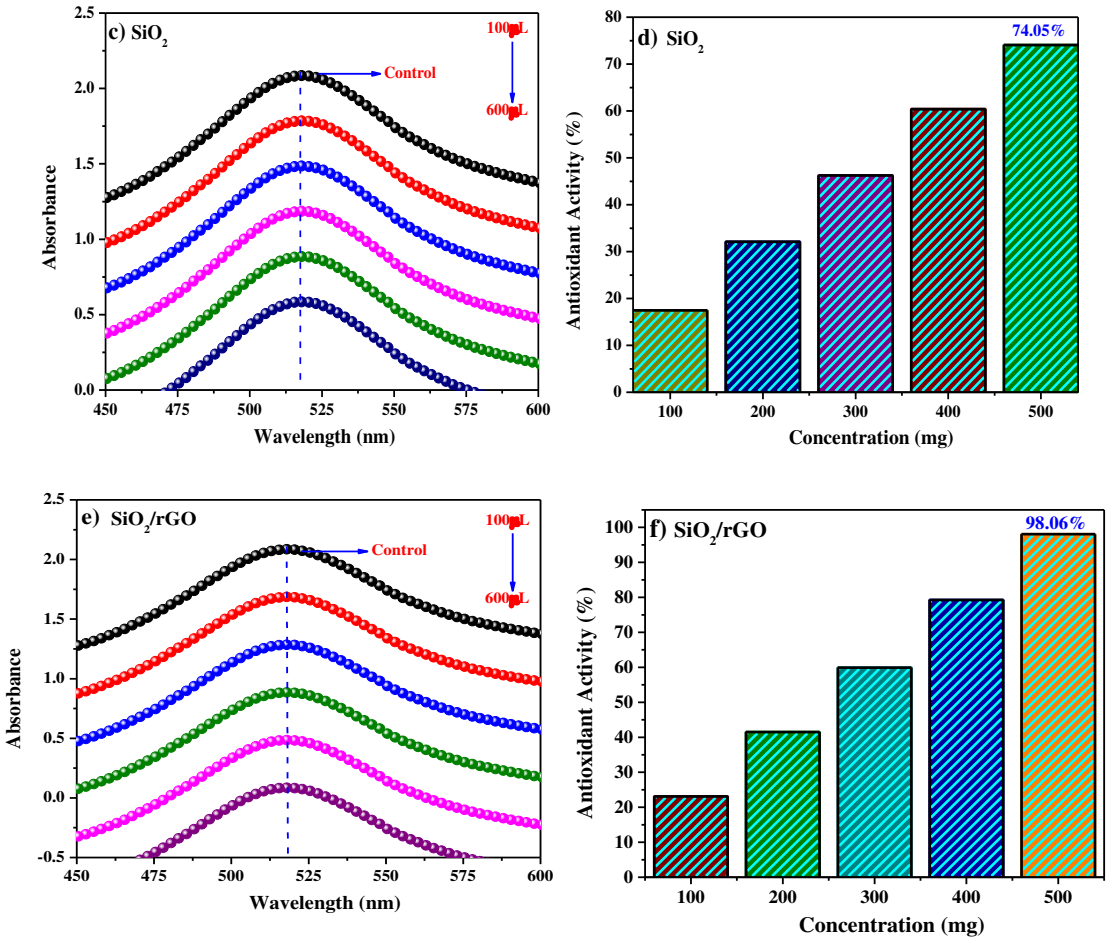

Fig. 8. (a, c, e) UV spectrum and antioxidant activity (b, d, f) of rGO, SiO_2 and SiO_2/rGO.

Table 3. Antioxidant activity and IC_{50} values of rGO.

Volume of extract (µL)	Volume of methanol (µL)	Concentration (µg)	Absorbance	% Activity	IC_{50} (mg/mL)
100	600	1000	1.86	12.36	
200	500	2000	1.66	21.69	**488.359**
300	400	3000	1.45	31.60	
400	300	4000	1.26	40.56	
500	200	5000	1.04	50.94	
Control			**2.12**		

Table 4. Antioxidant activity and IC_{50} values of SiO_2.

Volume of extract (µL)	Volume of methanol (µL)	Concentration (µg)	Absorbance	% Activity	IC_{50} (mg/mL)
100	600	1000	1.75	17.45	**329.419**
200	500	2000	1.44	32.07	
300	400	3000	1.14	46.22	
400	300	4000	0.84	60.37	
500	200	5000	0.55	74.05	
Control			**2.12**		

Table 5. Antioxidant activity and IC_{50} values of SiO_2/rGO.

Volume of extract (µL)	Volume of methanol (µL)	Concentration (µg)	Absorbance	% Activity	IC_{50} (mg/mL)
100	600	1000	1.63	23.11	**248.368**
200	500	2000	1.24	41.50	
300	400	3000	0.85	59.90	
400	300	4000	0.44	79.24	
500	200	5000	0.041	98.06	
Control			**2.12**		

The methods for assessing antioxidant activity and calculating the IC_{50} value are explained in Tables 3, 4, and 5. The radical scavenging capabilities of rGO (488.359 mg/mL), SiO_2 (329.419 mg/mL), and SiO_2/rGO nanocomposites (248.368 mg/mL) are presented in Tables 3, 4, and 5 and illustrated in Fig. 8. The optimal antioxidant effectiveness, a lower IC_{50} value is preferable. The half-scavenging efficiency (IC_{50}) represents the concentration at which half of the free radicals are neutralized by the sample, indicating its potency. rGO, SiO_2, and SiO_2/rGO nanocomposites can efficiently neutralize DPPH free radicals by donating electrons to oxygen atoms. This interaction results in the formation of a stable DPPH molecule, causing the initial pink color of the methanol-

based DPPH solution to diminish [102-103]. The comparative study of antioxidant activity by various metal oxides is shown in Table 6.

Table 6. Comparative study of Antioxidant activity by various metal oxides.

Nanomaterial	Antioxidant activity (%)	IC_{50} (mg/mL)	Reference
Clay/RuO_2	91	112.11	[14]
Honey/CeO_2	63.22	326.79	[26]
Pd-rGO-ZnO	58.0	-	[91]
rGO/MgO	82.67	2609.233	[92]
rGO/Fe_3O_4/Chitosan	87.6	-	[93]
Au NPs	92.34	0.04025	[95]
MgO NPs	76.59	0.5	[96]
ZnO	73	46.5	[97]
CeO_2	97	-	[98]
SiO_2@Ag@LA	33	-	[99]
SiO_2/rGO	**98.06**	**248.368**	**Present Work**

2.7. CV studies

The cyclic voltammetry (CV) graphs of prepared rGO, SiO_2 and doped SiO_2/rGO electrodes are shown in Fig. 9. The experiments encompassed of scan rates range from 5 to 50 mVs^{-1}. The steady current response for rGO, SiO_2, and doped SiO_2/rGO in a 1M KCl electrolyte indicated in Table 8, 9 and 10 respectively. In this analysis, it's evident that both rGO and SiO_2 exhibit cathodic and anodic peak currents when associated to SiO_2/rGO as illustrated in Fig. 9 (b, d, f). The regression value (R^2) for the SiO_2/rGO nanocomposite is significantly improved at 0.9944, in contrast to R^2 values of 0.9810 for rGO and 0.9956 for SiO_2. These values indicate a redox reaction of the electrodes that is both reversible and diffusion-controlled [102-103]. Nevertheless, its crucial to emphasize that there is no substantial enhancement in the variation current as the scan rates increase for both rGO and SiO_2 graphs. The final results showed in the inset of Fig. 9 ((a) (i)), 9

((c) (i)), and 9 ((e) (i)) illustrate is a direct correlation between variations in the redox peak potentials (E_0-E_R) magnitude and the square root of the scan rate.

This demonstrates efficient charge transfer kinetics at the interface between the electrode and the electrolyte medium, where E_R and E_0 represent the anodic and cathodic peaks potential. In eq. (13) depicts the appropriate reduction and oxidation mechanism occurring within the system.

$$SiO_2 + H_3O^+ + e^- \rightarrow Si + H_2O + O_2 \ldots\ldots\ldots\ldots\ldots\ldots\ldots\ldots (13)$$

Silica oxide (SiO_2) is reduced by the H_2 ion, acquiring an electron to produce silicon. Simultaneously, the hydrated H_2 ion is oxidized by dropping an electron, resulting in the formation of H_2O and O_2 gas [102]. This process is a redox reaction, involving the transfer of electrons from one to another reactant. In accordance, with the Randles-Sevcik relation, which governs reversible methods, the increase in present current is expressed in eq. (14) [103],

$$i_p = 2.69 \times 10^5 \times n^{\frac{3}{2}} \times A \times D^{\frac{1}{2}} \times C_0 \times v^{\frac{1}{2}} - - - -(14)$$

In this above equation, 'n' denotes the number of electrons, 'A' denotes the surface area, 'v' is the scan rate, 'D' signifies the diffusion coefficient, and 'C_0' represents the concentration of the material. The linear correlation observed the peaks current (i_p) and the square root of the number of electrons moved ($n^{1/2}$) serves as evidence that the final electrode reactions of rGO, SiO_2, and SiO_2/rGO were investigated with respect to the proton diffusion coefficient (D) were indicated in Tables 7, 8 and 9 respectively. The elevated D value of SiO_2/rGO indicates that its electrochemical reaction activity is more efficient when compared to rGO and SiO_2. The specific capacitance and final electrode surface area of rGO, SiO_2, and SiO_2/rGO were determined relation (15) based on the CV method [104].

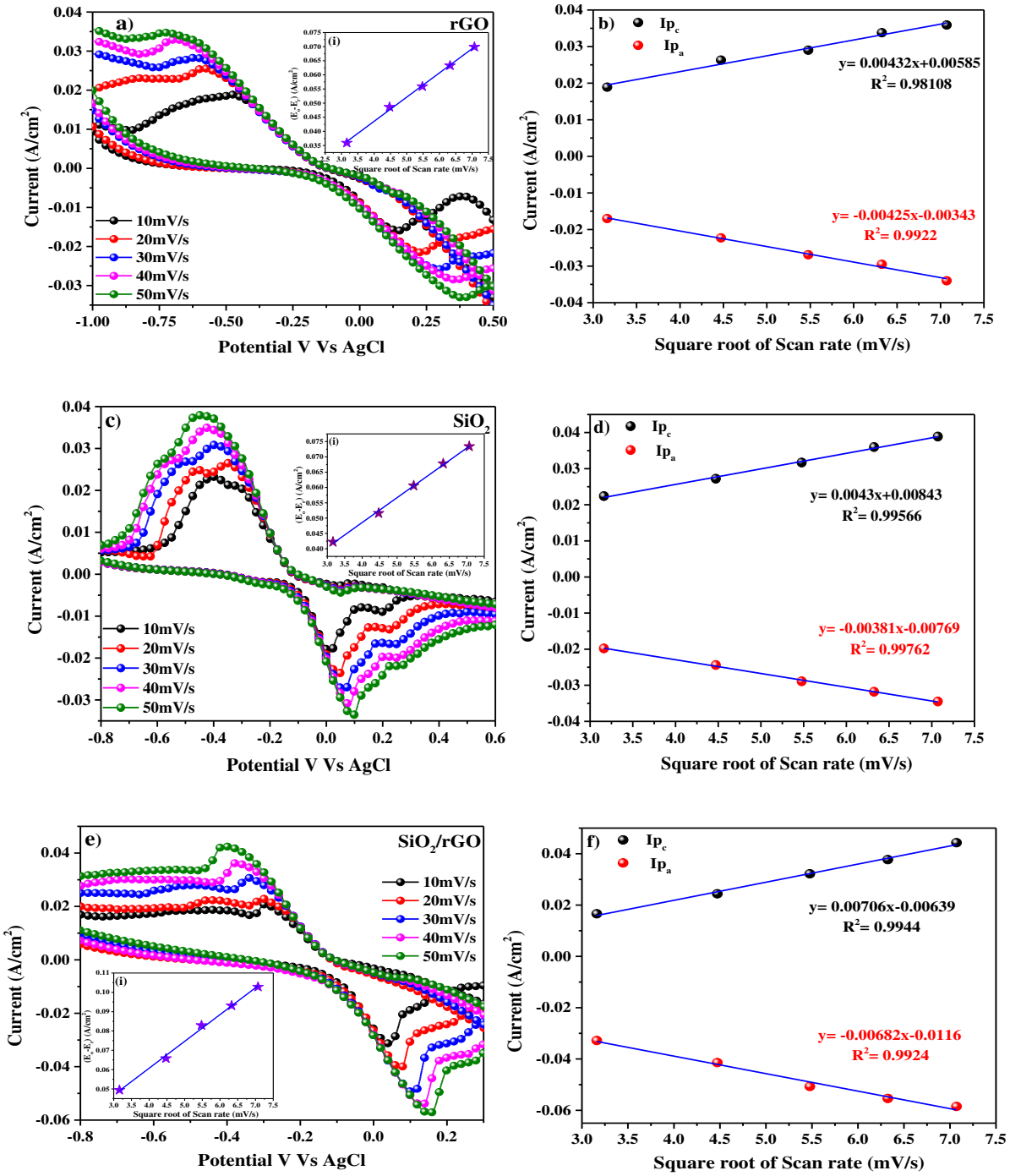

Fig. 9. CV curves (a, c, e) and square root of scan rate (b, d, f) of rGO, SiO_2 and SiO_2/rGO.

$$C_{sp} = \frac{A}{2mk(V_1 - V_2)} \ldots\ldots\ldots\ldots\ldots\ldots\ldots\ldots\ldots (15)$$

Where C_{sp} represents the specific capacitance, 'm' denotes the mass of the active material in grams, 'k' stands for the scan rate in volts, 'V_1' and 'V_2' indicate the initial and final potential window, and

'A' represents the surface area. The specific capacitance (Csp) values for rGO, SiO_2, and SiO_2/rGO were determined to be 75, 96, and 114 F/g were indicated in Tables 7, 8 and 9 respectively. The SiO_2/rGO nanocomposite demonstrates a significantly higher capacitance value when compared to rGO and SiO_2. Moreover, the surface concentration of the electrodes (rGO, SiO_2, and SiO_2/rGO) was investigated using the Brown-Anson eq. (16) [105-106].

$$I_P = n^2 F^2 Z Av (4RT)^{-1} \qquad (16)$$

In this equation, 'ip' denotes the peak current of the electrode, 'n' represents the number of electrons transferred (for KCl, n = 1), 'F' is the Faraday constant (96485 C mol^{-1}), 'A' is the electrode surface area (1 cm^2), 'R' is the gas constant (8.314 J $mol^{-1}K^{-1}$), 'v' is the scan rate (V/s), 'T' stands for room temperature (298K or 25 °C), and 'Z' is the surface concentration of the electrode. The surface concentration of the electrodes was determined to be 2.09 x 10^{-9} mol cm^{-2} for rGO, 2.56 x 10^{-9} mol cm^{-2} for SiO_2, and 2.66 x 10^{-9} mol cm^{-2} for SiO_2/rGO. Based on these results, it is evident that the SiO_2/rGO nanocomposite exhibited a significantly higher surface concentration in comparison to both rGO and SiO_2 [107-109].

A greater surface concentration of an electrode indicates a higher accumulation of relevant species at the electrode's interface. This increased concentration usually correlates with improved electrochemical reactivity and reaction rates, especially at the electrode surface where numerous catalytic and redox processes occur. The increased availability of reactants or catalysts enhances the efficiency of charge transfer reactions, catalytic activity, and sensing capabilities in electrochemical systems [110-112].

Table 7. Reversibility, proton diffusion coefficient and capacitance of rGO.

Scan rates (mV/s)	E_0 (V)	E_R(V)	E_0-E_R(V)	D×10^{-3}	C_{sp} (F/g)
10	0.0189	0.017	0.0359		
20	0.0263	0.0223	0.0486	4.32	
30	0.0290	0.0269	0.0559		75
40	0.0338	0.0295	0.0633	-4. 25	
50	0.0359	0.0341	0.0700		

Table 8. Reversibility, proton diffusion coefficient and capacitance of SiO_2.

Scan rates (mV/s)	E_0 (V)	E_R(V)	E_0-E_R(V)	D×10^{-3}	C_{sp} (F/g)
10	0.0224	0.0198	0.0422		
20	0.0272	0.0244	0.0516	4.3	
30	0.0317	0.0289	0.0606		96
40	0.036	0.0318	0.0678	-3.81	
50	0.0389	0.0345	0.0734		

Table 9. Reversibility, proton diffusion coefficient and capacitance of SiO_2/rGO.

Scan rates (mV/s)	E_0 (V)	E_R(V)	E_0-E_R(V)	D×10^{-3}	C_{sp} (F/g)
10	0.0166	0.0328	0.0494		
20	0.0244	0.0414	0.0658	0.7.06	
30	0.0322	0.0507	0.0829		114
40	0.0377	0.0554	0.0931	-6.82	
50	0.0443	0.0585	0.1028		

2.8. Voltammetry sensor

The ability of rGO, SiO_2, and SiO_2/rGO nickel mesh electrode to sense the various concentration of bee pollen and cow urine (1-7 mM) were analyzed through CV as shown in the Fig.10 a) to Fig.10 (f). In Fig. 10 (a) and 10 (b) shows sensing performance of bee pollen and cow urine using rGO electrode in the potential range between -1.0 to -0.5V. This shows increase in the current (+ 0.0251 A/cm^2 at 7 mM) for bee pollen and for cow urine sensor shows an increase current in the potential range between range between -0.8 to -0.2V about (+ 0.02565 A/cm^2 at 7 mM) [45]. Fig. 10 (c) and 10 (d) are shows the sensing performance of bee pollen and cow urine using SiO_2 electrode in the potential range between -0.75 to -0.35V showing an increase in the current (+ 0.0523 A/cm^2 at 7 mM) for bee pollen and for cow urine sensor which displays an increased current in the potential range between -0.70 to -0.30V about (+ 0.02565 A/cm^2 at 7 mM). Fig. 10 (e) and 15 (f) demonstrates the sensing measurement of bee pollen and cow urine using SiO_2/rGO electrode in the potential range between -0.70 to -0.30V displaying an increase in the current (+ 0.0471 A/cm^2 at 7 mM) for bee pollen and for cow urine sensor shows an increased current in the potential range between -0.70 to -0.30V about (+0.0500 A/cm^2 at 7 mM) [24, 50, 51]. The above obtained results show that the rGO/SiO_2 electrode exhibit good sensing property towards bee pollen and cow urine sensor material in the same potential scale window and showing high current response.

Table 10. LOD and LOQ values of rGO, SiO_2 and SiO_2/rGO.

Sample	**Bee pollen**		**Cow urine**	
	LOD (mM)	**LOQ (mM)**	**LOD(mM)**	**LOQ (mM)**
rGO	2.99	9.06	4.18	12.67
SiO_2	1.71	5.20	2.58	7.84
SiO_2/rGO	2.84	8.62	2.45	7.44

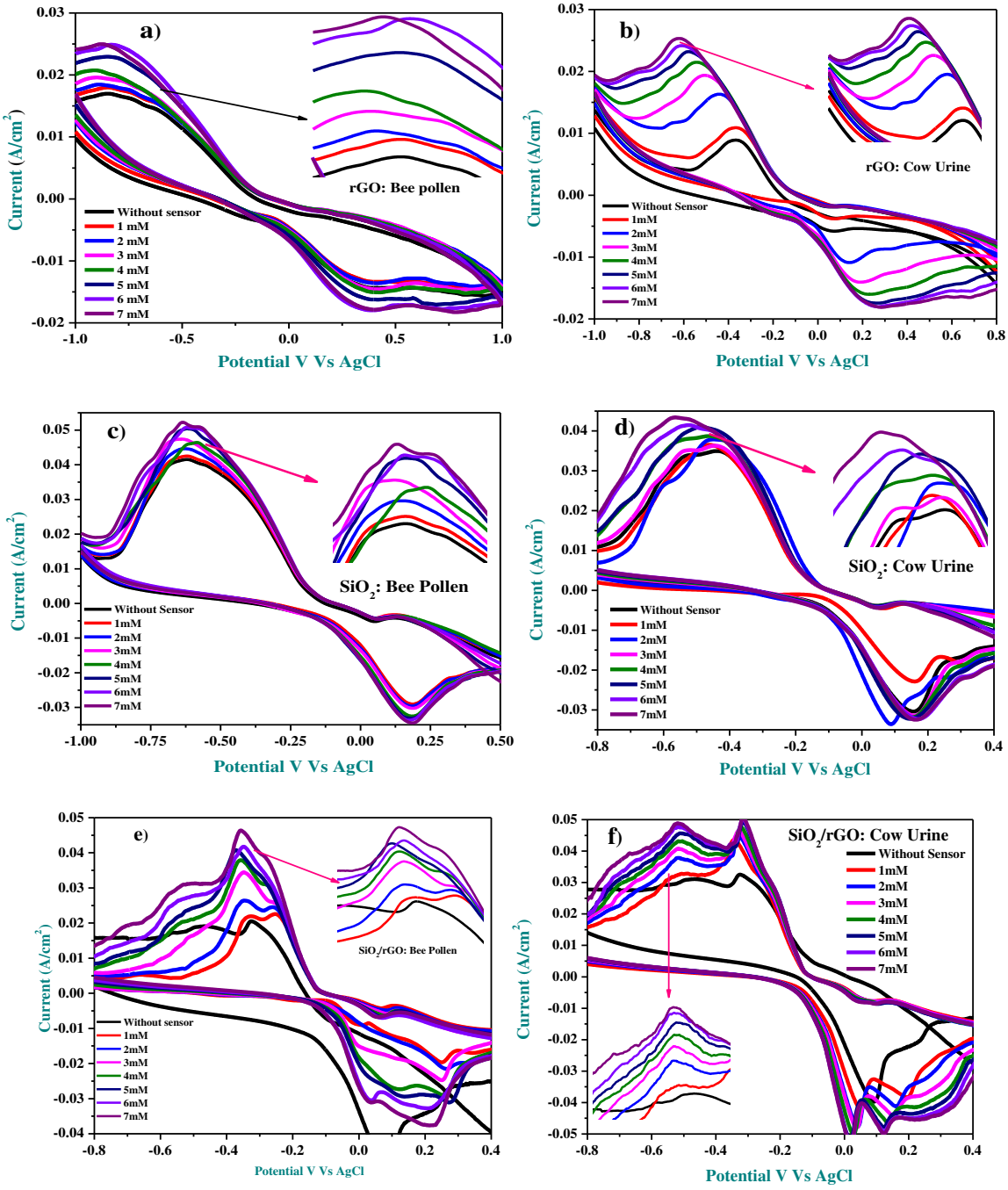

Fig.10. (a, b, c, d, e, f) CV sensor response curves of bee pollen and cow urine in rGO, SiO_2 and SiO_2/rGO.

A calibration graph was plotted in the relationship between the concentration of the sensor (mM) and its peak current of the sensor shown in Fig.11 a) to Fig.11 c) and various parameters of the sensors are represented in the Table 10. The sensitivity of the materials was found by the slope of

the graph by the active area of the electrode was found 0.00398 (bee pollen) and 0.00267 (cow urine) A/mM/cm^2 for SiO_2/rGO which is greater as compared to the rGO and SiO_2. The Limit of detection (LOD) and limit of quantification (LOQ) were calculated using eq. (17) and (18) [26].

$$\mathbf{LOD} = 3.3\left(\frac{\delta}{\mathrm{m}}\right) \ldots\ldots\ldots\ldots\ldots\ldots\ldots\ldots (17)$$

$$\mathrm{LOQ} = 10\left(\frac{\delta}{\mathrm{m}}\right) \ldots\ldots\ldots\ldots\ldots\ldots\ldots\ldots (18)$$

Where, 'δ' is the standard deviation and 'm' is the slope of the calibration curve.

LOD and LOQ determined from CV were given in Table 10 for rGO, SiO_2, and SiO_2/rGO electrodes.

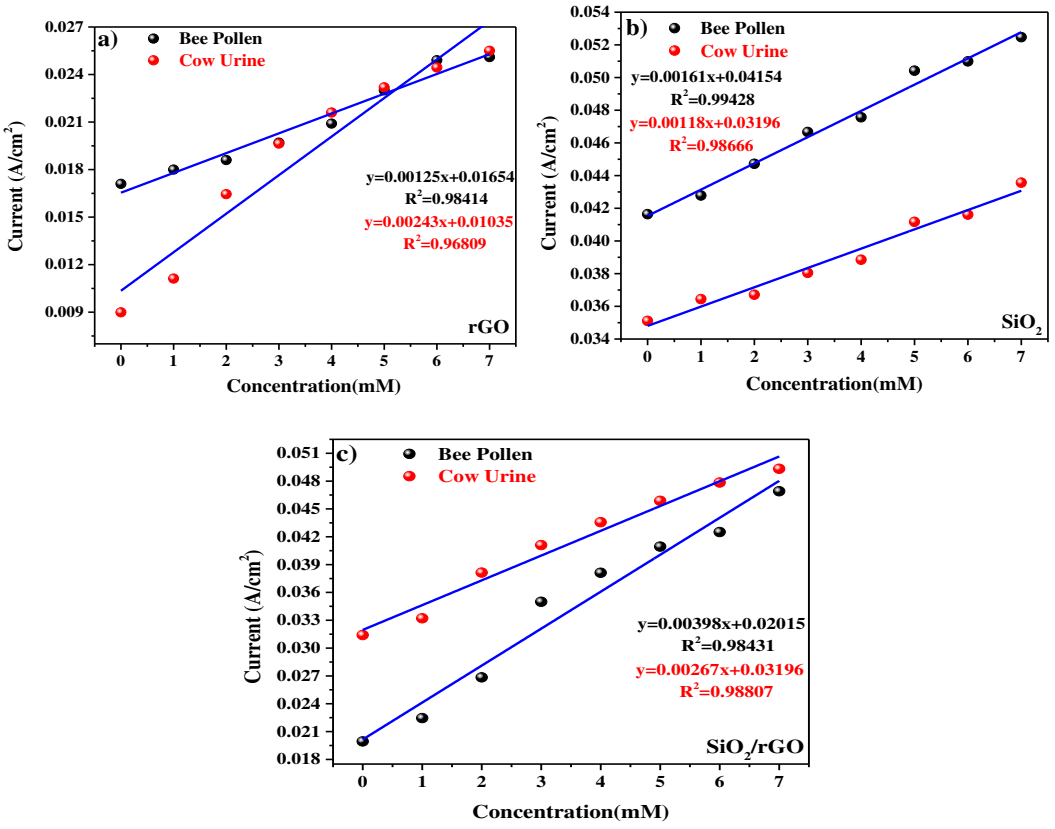

Fig. 11. A calibration graphs (a, b, c) of rGO, SiO_2 and SiO_2/rGO.

2.9. Reproducibility and Stability of Electrodes

The reproducibility and stability of the nickel mesh electrode are shown in Fig. S3. The reproducibility of nanomaterials (rGO, SiO_2 and SiO_2/rGO) for 800 cycles at 50 mV/s were demonstrated in Fig. S3 (a-c) respectively. The stability of the nanomaterial (rGO, SiO_2 and SiO_2/rGO) was tested for 25^{th} day cycle in the 0.1M KCl (pH~7) shown in the Fig. S3 and excellent results were recorded. The SiO_2/rGO have a good reproducibility, as evidenced by low relative standard deviation (RSD) of 1.31 % as compared to rGO (3.78 %) and SiO_2 (2.46 %), this confirms a reliability of the SiO_2/rGO sensor [74]. Based on the absence of significant difference. It can be considered a working electrode for sensing of bee pollen and cow urine using nickel mesh electrode [14, 23].

2.10. Selectivity test

During the construction of biosensor devices, selectivity plays a pivotal role in their operation. It furnishes details regarding the capability to accurately identify the target analyte in a mixture. The research encompassed the investigation of species exhibiting similar oxidation potential and chemical characteristics as chemicals, in addition to the most frequently encountered compounds in natural products [100]. The selectivity analysis involves a comparison between various organic acids and different fruit juices, including Goat urine, Bee wax, Horse urine, Bee pollen, Cow urine, Honey, Human urine and Bee venom. For this analysis, a solution of prepared chemicals (1 mM) and the natural product (approximately 1 drops or 1 ml) were introduced into the electrolyte with a concentration of 1M KCl. The current response obtained from the Differential Pulse Voltammetry (DPV) demonstrates the highest current within the potential range from -1.0 to 1.0 V. Based on the analysis, we can draw the conclusion that Bee pollen and Cow urine, exhibits effective detection capabilities. As a result, it has been selected for further examination, as depicted in Fig. 12 (d)

[102]. The research work incorporated the use of differential pulse voltammetry (DPV) analysis conducted on a nickel mesh electrode modified with SiO_2/rGO. The purpose was to evaluate the storage stability of a 3 mM solution comprising bee pollen and cow urine, which was dissolved in a 1 M KCl solution at a pH level of around 7. The biosensor, which had been prepared, was stored at room temperature (25°C). After 60 days, the recorded current response remained constant at approximately 100% for both sensors. However, after 40 days, the current response declined to 70 % of its initial value. The biosensor's stability is defined as achieving 90 % of the initial response within 20 days. Furthermore, the sensitivity of the sensor was determined by calculating the slope of the linearity graph and dividing it by the active area. The sensitivity values were determined to be 8.0595×10^{-5} A mM^{-1} cm^{-2} for Bee pollen and 8.0357×10^{-5} A mM^{-1} cm^{-2} for Cow urine. The linear range of the prepared sensor material was explored within the range of 1 to 7 mill molar.

2.11. DPV sensor studies

The correlation between different concentrations of Bee pollen and Cow urine and the peak current was determined using the Differential Pulse Voltammetry (DPV) method. The nickel mesh electrode modified with rGO, SiO_2 and SiO_2/rGO was employed to detect various concentrations of Bee pollen and Cow urine ranging from 1 to 7 mM. The results indicate that the DPV curves exhibited a gradual increase in both current and concentrations of Bee pollen and Cow urine within different potential ranges spanning from -1.0 to 1.0 V [112]. A calibration graph was constructed, illustrating the relationship between the concentrations of Bee pollen and Cow urine and their respective peak currents. These graphs can be observed in Fig.12 (a-f) and Fig.13 (a-c). The plot reveals a linear relationship between the two distinct parameters, which is characterized by the slope, intercept, and regression value as detailed in Table 5. It is evident that the reduction current rises with an increase in both Bee pollen and Cow urine concentrations. The Limits of Detection

(LOD) and Limits of Quantification (LOQ) were determined using equations (17) and (18) shown in the Table. 11 [113].

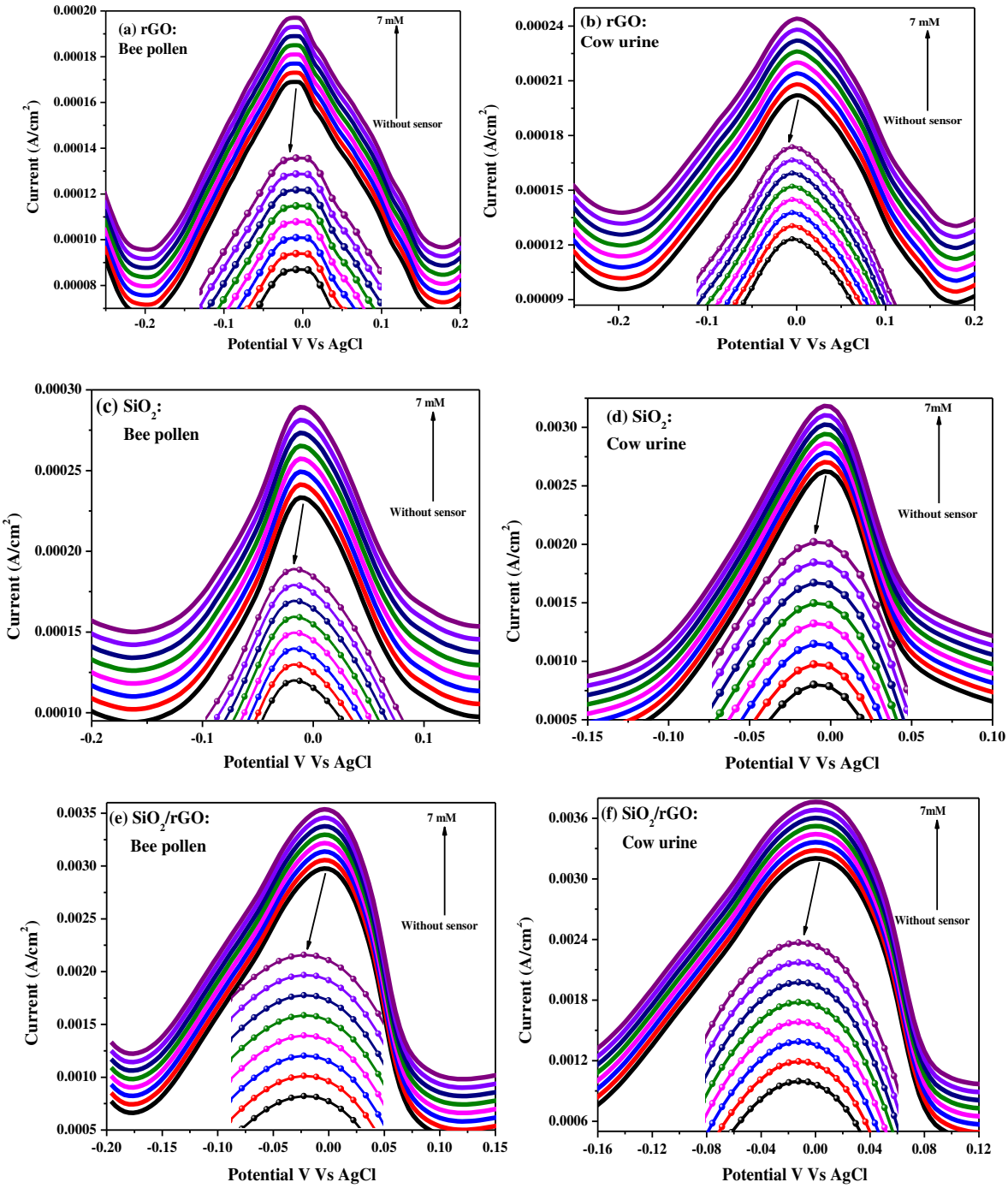

Fig. 12. (a-f) DPV of rGO, SiO_2 and SiO_2/rGO using Bee pollen and Cow urine.

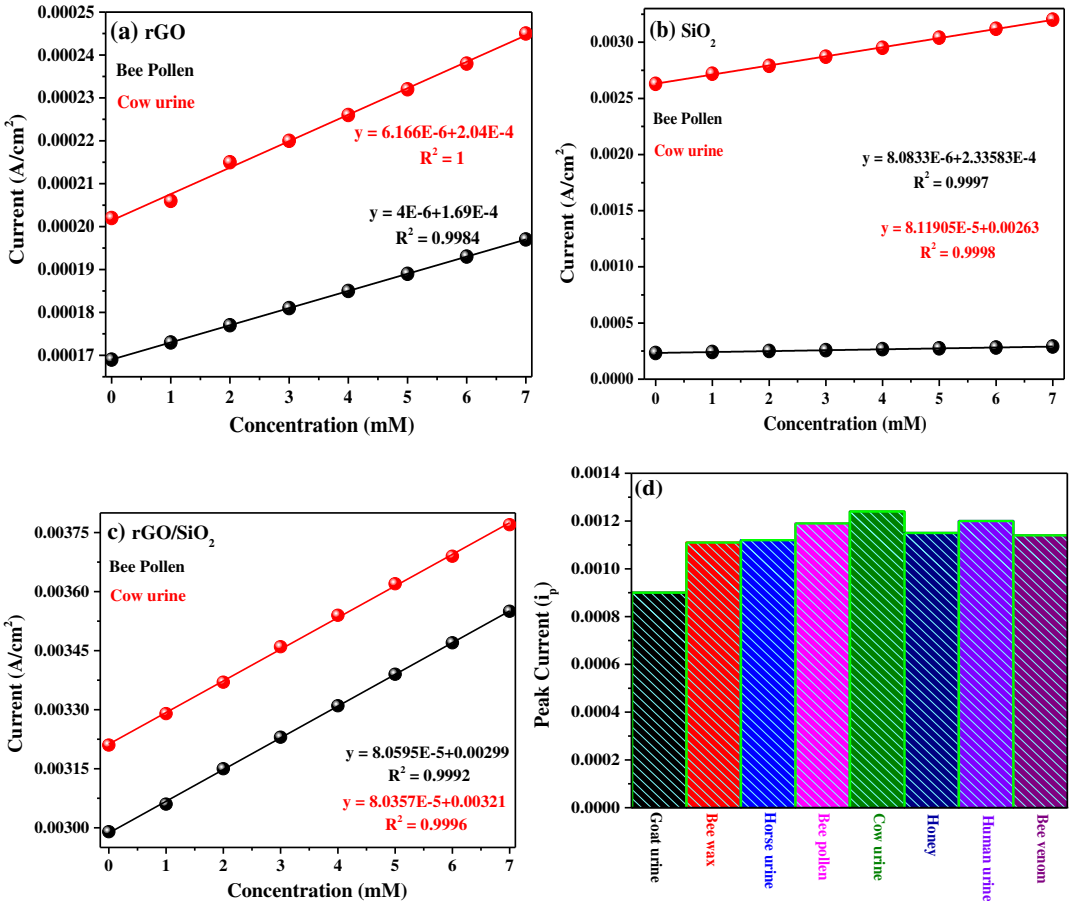

Fig. 13. (a-c) DPV of rGO, SiO_2 and SiO_2/rGO using Bee pollen and Cow urine and (d) Selectivity of the sensor.

Table 11. LOD and LOQ values DPV of rGO, SiO_2, and SiO_2/rGO.

Sample	Bee pollen		Cow urine	
	LOD (mM)	LOQ (mM)	LOD (mM)	LOQ (mM)
rGO	0.212	0.682	0.876	2.657
SiO_2	0.232	0.704	0.359	1.088
SiO_2/rGO	0.260	0.788	0.413	1.25

Conclusion

The synthesized compound was assessed for its photocatalytic activity against malachite green, signifying a remarkably pronounced catalytic efficiency (97%) compared to that of rGO and SiO_2.The DPPH free radical scavenging assay was employed to evaluate the antioxidant activity

of rGO, SiO_2 and SiO_2/rGO, revealing a 98 % activity level and an IC_{50} value of 488.35 mg/mL. This specifies the compound capability to neutralize free radicals effectively, which is indicative of its potential as an antioxidant agent. The electrochemical inspection was shown that SiO_2/rGO had higher cycle reversibility, proton diffusion coefficient and specific capacitance. The sensing action was carried out with bee pollen and cow urine, resulting in the identification of current peaks in both the oxidation and reduction reactions. Conferring to the outcomes, the material SiO_2/rGO is the more promising and effective material in the investigation of other biomolecules, industry pollutants and pharmaceutical samples. This method provides an environmentally friendly way of producing SiO_2/rGO which could be used for potential applications in various fields such as energy storage, catalysis, biomedical, and sensor studies.

CRediT author statement

Swetha N: Experimental, Data Collection and Writing **Dr. Venkata Lakshmi V:** Visualization, Investigation, **Dr. Mylarappa M**: Supervision, **Chandruvasan S**: Characterization Techniques, conceptualization, **Harisha K S:** review and editing:

Declaration of Competing Interest: The authors declare that they have no known competing financial interests or personal relationships that could have appeared to influence the work reported in this paper.

Data availability: No data was used for the research described in the article.

References

[1] Chen, G., Du, G., Ma, W., Yan, B., Wang, Z., and Gao, W. (2015). Production of amorphous rice husk ash in a 500kW fluidized bed combustor. Fuel *144*, 214–221. https://doi.org/10.1016/j.fuel.2014.12.012 .

[2] Fernandes, I.J., Calheiro, D., Kieling, A.G., Moraes, C.A.M., Rocha, T.L.A.C., Brehm, F.A., and Modolo, R.C.E. (2016). Characterization of rice husk ash produced using different biomass combustion techniques for energy. Fuel *165*, 351–359. https://doi.org/10.1016/j.fuel.2015.10.086.

[3] Azat, S., Korobeinyk, A.V., Moustakas, K., and Inglezakis, V.J. (2019). Sustainable production of pure silica from rice husk waste in Kazakhstan. Journal of Cleaner Production *217*, 352–359. https://doi.org/10.1016/j.jclepro.2019.01.142.

[4] Rozainee, M., Ngo, S., Salema, A., Tan, K., Ariffin, M., and Zainura, Z. (2008). Effect of fluidising velocity on the combustion of rice husk in a bench-scale fluidised bed combustor for the production of amorphous rice husk ash. Bioresource Technology *99*, 703–713. https://doi.org/10.1016/j.biortech.2007.01.049.

[5] Mohammed, R.H., Mesalhy, O., Elsayed, M.L., Hou, S., Su, M., and Chow, L.C. (2018). Physical properties and adsorption kinetics of silica-gel/water for adsorption chillers. Applied Thermal Engineering *137*, 368–376. https://doi.org/10.1016/j.applthermaleng.2018.03.088.

[6] Bakar, R.A., Yahya, R., and Gan, S.N. (2016). Production of high purity amorphous silica from rice husk. Procedia Chemistry *19*, 189–195. https://doi.org/10.1016/j.proche.2016.03.092.

[7] Kerimkulova, A.R., Azat, S., Mansurov, Z.A., Gilmanov, M.K., Ibragimova, S.A., Adekenov, S.M., and Rachimova, B.B. (2012). Mesoporous nano carbon sorbents for separating different biomolecules. AMR *535–537*, 284–288. https://doi.org/10.4028/www.scientific.net/AMR.535-537.284.

[8] Azat, S., Pavlenko, V.V., Kerimkulova, A.R., and Mansurov, Z.A. (2012). Synthesis and structure determination of carbonized nano mesoporous materials based on vegetable raw materials. AMR *535–537*, 1041–1045. 10.4028/www.scientific.net/AMR.535-537.1041.

[9] Prasara, A, J., and Gheewala, S.H. (2017). Sustainable utilization of rice husk ash from power plants: A review. Journal of Cleaner Production *167*, 1020–1028. https://doi.org/10.1016/j.jclepro.2016.11.042.

[10] Chukwudebelu, J.A., Igwe, C.C., and Madukasi, E.I. (2015). Prospects of using whole rice husk for the production of dense and hollow bricks. African Journal Environmental Science and Technology, *9*, 493–501. https://doi.org/10.5897/AJEST2013.1631.

[11] Hegazi, H.A. (2013). Removal of heavy metals from wastewater using agricultural and industrial wastes as adsorbents. HBRC Journal *9*, 276–282. https://doi.org/10.1016/j.hbrcj.2013.08.004.

[12] Ang, T.N., Ngoh, G.C., Chua, A.S.M., and Lee, M.G. (2012). Elucidation of the effect of ionic liquid pretreatment on rice husk via structural analyses. Biotechnology for Biofuels and Products, *5*, 67. https://doi.org/10.1186/1754-6834-5-67.

[13] Tayyab, M. (2018). Bioethanol production from lignocellulosic biomass by environment-friendly pretreatment methods: a review. Applied Ecology and Environmental Research *16*, 225–249. https://doi.org/10.15666/aeer/1601_225249.

[14] Mylarappa, M., Chandruvasan, S., Harisha K.S., and Sharath S. (2024). Synthesis characterization, and electrochemical detection of tartaric acid and grape juice using rGO doped La_2O_3 nanoparticles. Materials Science and Engineering B *299,* 116977(1-12). https://doi.org/10.10.1016/j.mseb.2023.116977.

[15] Chandrasekhar, S., Satyanarayana, K.G., Pramada, P.N., Raghavan, P., and Gupta, T.N. (2003). Review processing, properties and applications of reactive silica from rice husk-an overview. Journal of Materials Science *38*, 3159–3168. https://doi.org/10.1023/A:1025157114800.

[16] Novoselov, K.S., Geim, A.K., Morozov, S.V., Jiang, D., Zhang, Y., Dubonos, S.V., Grigorieva, I.V., and Firsov, A.A. (2004). Electric field effect in atomically thin carbon films. Science *306*, 666–669. https://doi.org/10.1126/science.1102896.

[17]Geim, A.K. (2009). Graphene: status and prospects. Science *324*, 1530–1534. https://doi.org/10.1126/science.1158877.

[18] Geim, A.K., and Novoselov, K.S. (2007). The rise of graphene. Nature Materials *6*, 183–191. https://doi.org/10.1038/nmat1849.

[19] Li, X., Wang, X., Zhang, L., Lee, S., and Dai, H. (2008). Chemically derived, ultrasmooth graphene nanoribbon semiconductors. Science *319*, 1229–1232. https://doi.org/10.1126/science.1150878.

[20] Meric, I., Han, M.Y., Young, A.F., Ozyilmaz, B., Kim, P., and Shepard, K.L. (2008). Current saturation in zero-bandgap, top-gated graphene field-effect transistors. Nature Nanotechnology *3*, 654–659. https://doi.org/10.1038/nnano.2008.268.

[21] Avouris, P., Chen, Z., and Perebeinos, V. (2007). Carbon-based electronics. Nature Nanotechnology *2*, 605–615. https://doi.org/10.1038/nnano.2007.300.

[22] Liang, M., and Zhi, L. (2009). Graphene-based electrode materials for rechargeable lithium batteries. Journal of Materials Chemistry *19*, 5871. https://doi.org/10.1039/b901551e.

[23] Stoller, M.D., Park, S., Zhu, Y., An, J., and Ruoff, R.S. (2008). Graphene-based ultracapacitors. Nano Letters *8*, 3498–3502. https://doi.org/10.1021/nl802558y.

[24] E., Kim, J., Hosono, E., Zhou, H., Kudo, T., and Honma, I. (2008). Large reversible Li storage of graphene nanosheet families for use in rechargeable lithium ion batteries. Nano Letters *8*, 2277–2282. https://doi.org/10.1021/nl800957b.

[25] Zhang, M., Yin, B.C., Tan, W., and Ye, B.C. (2011). A versatile graphene-based fluorescence "on/off" switch for multiplex detection of various targets. Biosensors and Bioelectronics *26*, 3260–3265. https://doi.org/10.1016/j.bios.2010.12.037.

[26] Mylarappa, M., Chandruvasan, S., Harisha, K.S., Kantharaju, S., Prasanna Kumar, S.G., and Shravana Kumara, K.N. (2023). Development of Coriander Honey loaded CeO_2 for cyclic voltammetry, chemical sensor, dye purification, and antioxidant properties. Journal of the Taiwan Institute of Chemical Engineers *152*, 105174. https://doi.org/10.1016/j.jtice.2023.105174.

[27] Fowler, J.D., Allen, M.J., Tung, V.C., Yang, Y., Kaner, R.B., and Weiller, B.H. (2009). Practical chemical sensors from chemically derived graphene. ACS Nano *3*, 301–306. https://doi.org/10.1021/nn800593m.

[28] Sherlock, S.P., Tabakman, S.M., Xie, L., and Dai, H. (2011). Photothermally enhanced drug delivery by ultrasmall multifunctional FeCo/graphitic shell nanocrystals. ACS Nano *5*, 1505–1512. https://doi.org/10.1021/nn103415x.

[29] Wang, J., Zhao, H., He, J., Wang, C., and Wang, J. (2011). Nano-sized SiOx/C composite anode for lithium ion batteries. Journal of Power Sources *196*, 4811–4815. https://doi.org/10.1016/j.jpowsour.2011.01.053.

[30] Chan, C.K., Peng, H., Liu, G., McIlwrath, K., Zhang, X.F., Huggins, R.A., and Cui, Y. (2008). High-performance lithium battery anodes using silicon nanowires. Nature Nanotech *3*, 31–35. https://doi.org/10.1038/nnano.2007.411.

[31] Park, C.M., Kim, J.H., Kim, H., and Sohn, H.J. (2010). Li-alloy based anode materials for Li secondary batteries. Chemical Society Review. *39*, 3115. https://doi.org/10.1039/b919877f.

[32] Tao, H., Fan, L.Z., Song, W.L., Wu, M., He, X., and Qu, X. (2014). Hollow core-shell structured Si/C nanocomposites as high-performance anode materials for lithium-ion batteries. Nanoscale *6*, 3138–3142. https://doi.org/10.1039/C3NR03090C.

[33] Hwa, Y., Park, C.M., and Sohn, H.J. (2013). Modified SiO as a high performance anode for Li-ion batteries. Journal of Power Sources *222*, 129–134. https://doi.org/10.1016/j.jpowsour.2012.08.060.

[34] Yan, N., Wang, F., Zhong, H., Li, Y., Wang, Y., Hu, L., and Chen, Q. (2013). Hollow Porous SiO_2 nanocubes towards high-performance anodes for lithium-ion batteries. Science Report *3*, 1568. https://doi.org/10.1038/srep01568.

[35] Favors, Z., Wang, W., Bay, H.H., George, A., Ozkan, M., and Ozkan, C.S. (2014). Stable cycling of SiO_2 nanotubes as high-performance anodes for lithium-ion batteries. Science Reports *4*, 4605. https://doi.org/10.1038/srep04605.

[36] Nguyen, C.C., Choi, H., and Song, S.W. (2013). Roles of oxygen and interfacial stabilization in enhancing the cycling ability of silicon oxide anodes for rechargeable lithium batteries. Journal Electrochemical Society *160*, A906–A914. https://doi.org/10.1149/2.118306jes.

[37] Li, W., Wang, F., Ma, M., Zhou, J., Liu, Y., and Chen, Y. (2018). Preparation of SiO_2 nanowire arrays as anode material with enhanced lithium storage performance. RSC Advance *8*, 33652–33658. https://doi.org/10.1039/C8RA06381H.

[38] Ojha, K., Kumar, B., and Ganguli, A.K. (2017). Biomass derived graphene-like activated and non-activated porous carbon for advanced supercapacitors. Journal of Chemical Science *129*, 397-404. https://doi.org/10.1007/s12039-017-1248-8.

[39] Hegab, H.M., ElMekawy, A., Zou, L., Mulcahy, D., Saint, C.P., and Ginic-Markovic, M. (2016). The controversial antibacterial activity of graphene-based materials. Carbon *105*, 362–376. https://doi.org/10.1016/j.carbon.2016.04.046.

[40] Yang, L., Wang, L., Xing, M., Lei, J., and Zhang, J. (2016). Silica nanocrystal/graphene composite with improved photoelectric and photocatalytic performance. Applied Catalysis B: Environmental *180*, 106–112. https://doi.org/10.1016/j.apcatb.2015.06.026.

[41] Alweendo, S.T., Johnson, O.T., Shongwe, M.B., Kavishe, F.P.L., and Borode, J.O. (2019). Synthesis, optimization and characterization of silicon carbide (SiC) from rice husk. Procedia Manufacturing *35*, 962–967. https://doi.org/10.1016/j.promfg.2019.06.042.

[42] Tuerhong, M., Xu, Y., and Yin, X.-B. (2017). Review on carbon dots and their applications. Chinese Journal of Analytical Chemistry *45*, 139–150. https://doi.org/10.1016/S1872-2040(16)60990-8.

[43] Arshad, A., Iqbal, J., Mansoor, Q., and Ahmed, I. (2017). Graphene/SiO_2 nanocomposites: The enhancement of photocatalytic and biomedical activity of SiO_2 nanoparticles by graphene. Journal of Applied Physics *121*, 244901. https://doi.org/10.1063/1.4979968.

[44] Chang, J.S., Chang, K.L.B., Hwang, D.F., and Kong, Z.L. (2007). *In vitro* cytotoxicitiy of silica nanoparticles at high concentrations strongly depends on the metabolic activity type of the cell line. Environmental Science and Technology *41*, 2064–2068. https://doi.org/10.1021/es062347t.

[45] Deligiannakis, Y., Sotiriou, G.A., and Pratsinis, S.E. (2012). Antioxidant and antiradical SiO_2 nanoparticles covalently functionalized with gallic acid. ACS Applied Materials Interfaces *4*, 6609–6617. https://doi.org/10.1021/am301751s.

[46] Alweendo, S.T., Johnson, O.T., Shongwe, M.B., Kavishe, F.P.L., and Borode, J.O. (2019). Synthesis, optimization and characterization of silicon carbide (SiC) from rice husk. Procedia Manufacturing *35*, 962–967. https://doi.org/10.1016/j.promfg.2019.06.042.

[47] Saceda, J.J.F., Leon, R.L.D., Rintramee, K., Prayoonpokarach, S., and Wittayakun, J. (2011). Properties of silica from rice husk and rice husk ash and their utilization for zeolite y synthesis. Quimica Nova *34*, 1394-97. https://doi.org/10.1590/S0100-40422011000800018.

[48] Thakur, S., and Karak, N. (2012). Green reduction of graphene oxide by aqueous phytoextracts. Carbon *50*, 5331–5339. https://doi.org/10.1016/j.carbon.2012.07.023.

[49] Cui, P., Lee, J., Hwang, E., and Lee, H. (2011). One-pot reduction of rGO at subzero temperatures. Chemical Communications. *47*, 12370. https://doi.org/10.1039/c1cc15569e.

[50] Ratsameetammajak, N., Autthawong, T., Chairuangsri, T., Kurata, H., Yu, A., and Sarakonsri, T. (2022). Rice husk-derived nano-SiO_2 assembled on reduced graphene oxide distributed on conductive flexible polyaniline frameworks towards high-performance lithium-ion batteries. RSC Advance, *12*, 14621–14630. https://doi.org/10.1039/D2RA00526C.

[51] Gu, N., Zhang, H., Ge, H., Wang, F., and Liu, B. (2021). *In-situ* polymerization of graphene/SiO_2 hybrids modified phenolic resin for improved thermal stability at an ultralow filler loading. Polymer Bulletin, *78*, 5963–5976. https://doi.org/10.1007/s00289-020-03409-8.

[52] Mylarappa, M., Raghavendra, N., Surendra, B.S., Shravana Kumar, K.N., and Kantharjau, S. (2022). Electrochemical, photocatalytic and sensor studies of clay/MgO nanoparticles. Applied Surface Science Advances *10*, 100268. https://doi.org/10.1016/j.apsadv.2022.100268.

[53] Chen, Z., Xu, Y., and Shivkumar, S. (2018). Microstructure and tensile properties of various varieties of rice husk: Microstructure and tensile properties of various varieties of rice husk. Journal of Science and Food Agriculture *98*, 1061-70. https://doi.org/10.1002/jsfa.8556.

[54] Stankovich, S., Piner, R.D., Nguyen, S.T., and Ruoff, R.S. (2006). Synthesis and exfoliation of isocyanate-treated graphene oxide nanoplatelets. Carbon *44*, 3342–3347. https://doi.org/10.1016/j.carbon.2006.06.004.

[55] Kim, D., Lee, S., and Piao, Y. (2017). Electrochemical determination of dopamine and acetaminophen using activated graphene-Nafion modified glassy carbon electrode. Journal of Electroanalytical Chemistry *794*, 221–228. https://doi.org/10.1016/j.jelechem.2017.04.018.

[56] Tian, L., Wang, X., Cao, L., Meziani, M.J., Kong, C.Y., Lu, F., and Sun, Y.-P. (2010). Preparation of bulk ^{13}C-Enriched graphene materials. Journal of Nanomaterials *2010*, 1–5. https://doi.org/10.1155/2010/742167.

[57] Dreyer, D.R., Murali, S., Zhu, Y., Ruoff, R.S., and Bielawski, C.W. (2011). Reduction of graphite oxide using alcohols. Journal of Material Chemistry. *21*, 3443–3447. https://doi.org/10.1039/C0JM02704A.

[58] Titelman, G.I., Gelman, V., Bron, S., Khalfin, R.L., Cohen, Y., and Bianco-Peled, H. (2005). Characteristics and microstructure of aqueous colloidal dispersions of graphite oxide. Carbon *43*, 641–649. https://doi.org/10.1016/j.carbon.2004.10.035.

[59] Leng, W., Chen, M., Zhou, S., and Wu, L. (2010). Capillary force induced formation of monodisperse polystyrene/silica organic-inorganic hybrid hollow spheres. Langmuir *26*, 14271–14275. https://doi.org/10.1021/la102256t.

[60] Ramezanzadeh, B., Haeri, Z., and Ramezanzadeh, M. (2016). A facile route of making silica nanoparticles-covered graphene oxide nanohybrids (SiO_2-GO); fabrication of SiO_2-GO/epoxy composite coating with superior barrier and corrosion protection performance. Chemical Engineering Journal *303*, 511–528. https://doi.org/10.1016/j.cej.2016.06.028.

[61] Mbakaan, C., Ahemen, I., Amah, A.N., Onojah, A.D., and Koao, L. (2018). White-light-emitting Dy^{3+}-doped amorphous SiO_2 nanophosphors derived from rice husk. Applied Physics A *124*, 741. https://doi.org/10.1007/s00339-018-2156-6.

[62] Adhikari, B.-R., Govindhan, M., Schraft, H., and Chen, A. (2016). Simultaneous and sensitive detection of acetaminophen and valacyclovir based on two dimensional graphene nanosheets. Journal of Electroanalytical Chemistry *780*, 241–248. https://doi.org/10.1016/j.jelechem.2016.09.023.

[63] Kaur, P., Kaur, P., and Kaur, K. (2020). Adsorptive removal of imazethapyr and imazamox from aqueous solution using modified rice husk. Journal of Cleaner Production *244*, 118699. https://doi.org/10.1016/j.jclepro.2019.118699.

[64] Srivastava, V.C., Mall, I.D., and Mishra, I.M. (2006). Characterization of mesoporous rice husk ash (RHA) and adsorption kinetics of metal ions from aqueous solution onto RHA. Journal of Hazardous Materials *134*, 257–267. https://doi.org/10.1016/j.jhazmat.2005.11.052.

[65] Patil, R., Dongre, R., & Meshram, J. (2014). Preparation of silica powder from raw rice husk. IOSR-Journal of Applied Chemistry, 27, 26-29. ISSN: 2278-5736.

[66] Im, Y.B., Wahab, R., Ameen, S., Kim, Y.S., Yang, O.B., and Shin, H.S. (2011). Synthesis and characterization of high-purity silica nanosphere from rice husk. Journal of Nanoscience and Nanotechnology, *11*, 5934–5938. https://doi.org/10.1166/jnn.2011.4386.

[67] Ferreira, C.S., Santos, P.L., Bonacin, J.A., Passos, R.R., and Pocrifka, L.A. (2015). Rice husk reuse in the preparation of SnO_2/SiO_2 nanocomposite. Material Research *18*, 639–643. https://doi.org/10.1590/1516-1439.009015.

[68] Gun, M., Arslan, H., Saleh, M., Yalvac, M., and Dizge, N. (2022). Optimization of silica extraction from rice husk using response surface methodology and adsorption of safranin dye. International Journal of Environmental Research *16*, 20. https://doi.org/10.1007/s41742-022-00399-5.

[69] Shetti, N.P., Malode, S.J., Nayak, D.S., Reddy, K.R., Reddy, C.V, and Ravindra, K. (2019). Silica gel-modified electrode as an electrochemical sensor for the detection of acetaminophen. Microchemical Journal *150*, 104206. https://doi.org/10.1016/j.microc.2019.104206.

[70] Tran, D.T., and Nguyen, V.N. (2020). Reduced graphene oxide/persulfate metal-free catalytic system for the degradation of tetracycline: effect of reaction parameters. Material Research Express *7*, 075501. https://doi.org/10.1088/2053-1591/ab9e47.

[71] Yusoff, F., Suresh, K., and Khairul, W.M. (2022). Synthesis and characterization of reduced graphene oxide/iron oxide/silicon dioxide ($rGO/Fe_3O_4/SiO_2$) nanocomposite as a potential cathode catalyst. Journal of Physics and Chemistry of Solids *163*, 110551. https://doi.org/10.1016/j.jpcs.2021.110551.

[72] Mylarappa, M., Chandruvasan, S., Thippeswamy, B., Shravana Kumara, K.N., and Kantharaju, S. (2023). Clay incorporated ruthenium oxide nanocomposite for electrochemical,

sensor, optical, photocatalytic and antioxidant studies. Sustainable Chemistry for the Environment *2*, 100007. https://doi.org/10.1016/j.scenv.2023.100007.

[73] Holgado, J.P., Alvarez, R., and Munuera, G. (2000). Study of CeO_2 XPS spectra by factor analysis: reduction of CeO_2. Applied Surface Science *161*, 301–315. https://doi.org/10.1016/S0169-4332(99)00577-2.

[74] Afza, N., Shivakumar, M.S., Alam, M.W., Kumar, A.N., Bhatt, A.S., Murthy, H.C.A., Ravikumar, C.R., Mylarappa, M., and Selvanandan, S. (2022). Facile hydrothermal synthesis of cerium oxide/rGO nanocomposite for photocatalytic and supercapacitor applications. Applied Surface Science Advances *11*, 100307. https://doi.org/10.1016/j.apsadv.2022.100307.

[75] Drabo, M., Budak, S., Egarievwe, S., and Lagle, R. (2021). XPS Studies of the SiO_2 substrates and thermoelectric thin films of $Sn/Sn^{+}SnO_2$ under the effects of the different thermal treatments. American Journal of Engineering and Applied Sciences *14*, 25–50. https://doi.org/10.3844/ajeassp.2021.25.50.

[76] Hernandez, A.L., Pujari, S.P., Laguna, M.F., Santamaría, B., Zuilhof, H., and Holgado, M. (2021). Efficient chemical surface modification protocol on SiO_2 transducers applied to MMP9 biosensing. Sensors *21*, 8156. https://doi.org/10.3390/s21238156.

[77] Li, W., l'Abee, R.M.A., and Goossens, J.G.P. (2013). The control of silica nanoparticles on the phase separation of poly(methyl methacrylate)/poly(styrene- *co* -acrylonitrile) blends. Macromolecualr Chemistry and Physics, *214*, 2705–2715. https://doi.org/10.1002/macp.201300475.

[78] Vinoda, B.M., Vinuth, M., Yadav, D. B, and Manjanna, J. (2015). Photocatalytic degradation of toxic methyl red dye using silica nanoparticles synthesized from rice husk ash. Journal of Environmental and Analytical Toxicology, *05*, 5-6 https://doi.org/10.4172/2161-0525.1000336.

[79] Lubis, S., Mustafa, I., Ermanda, Y., and Ramadhani, M. (2021). Preparation of SiO_2 /α-Fe_2O_3 composite from rice husk and iron sand as a photocatalyst for degradation of acid black dye. Journal of Physics: Conference Series *1819*, 012010. https://doi.org/10.1088/1742-6596/1819/1/012010.

[80] Ajayi, O. A., Okeniyi, O. O., Adekunle, O. A., and Sani, Y. M. (2021). Development and characterization of rice husk ash-based photocatalyst for degradation of methylene blue. Journal of Materials and Environmental Science, *12,* 1360-1372. ISSN: 2028-2508.

[81] Alhadhrami, A., Mohamed, G.G., Sadek, A.H., Ismail, S.H., Ebnalwaled, A.A., and Almalki, A.S.A. (2022). Behavior of silica nanoparticles synthesized from rice husk ash by the sol-gel method as a photocatalytic and antibacterial agent. Materials *15*, 8211. https://doi.org/10.3390/ma15228211.

[82] Wang, W., Chen, H., Fang, J., and Lai, M. (2019). Large-scale preparation of rice-husk-derived mesoporous SiO_2@TiO_2 as efficient and promising photocatalysts for organic contaminants degradation. Applied Surface Science *467–468*, 1187–1194. https://doi.org/10.1016/j.apsusc.2018.10.275.

[83] Eddy, D.R., Noviyanti, A.R., Solihudin, S., Ishmayana, S., and Tjokronegoro, R. (2017). Rice husk for photocatalytic composite material fabrication. In visible-light photo catalysis of carbon-based materials, Y. Yao, ed. (InTech). https://doi.org/10.5772/intechopen.72704.

[84] Chen, H., Zhao, L., Xiang, Y., He, Y., Song, G., Wang, X., and Liang, F. (2016). A novel Zn-TiO_2/$CaSiO_2$ nanoporous material on rice husk for photocatalytic applications under visible light. Desalination and Water Treatment *57*, 9660–9670. https://doi.org/10.1080/19443994.2015.1035339.

[85] Afzaal, A., and Farrukh, M.A. (2017). Zwitterionic surfactant assisted synthesis of Fe doped SnO_2-SiO_2 nanocomposite with enhanced photocatalytic activity under sun light. Materials Science and Engineering: B *223*, 167–177. https://doi.org/10.1016/j.mseb.2017.06.015.

[86] Nabeela Aslam, Farrukh, M.A., and Karim, S. (2019). Sensitization of Sm/SnO_2 SiO_2 nanocomposite with zwitterionic surfactant for enhanced photocatalytic performance under sunlight. Russian Journal of Physical Chemistry A *93*, 1610–1619. https://doi.org/10.1134/S0036024419080211.

[87] Rezai, P., Baniyaghoob, S., and Sadr, M.H. (2019). Fe_3O_4@SiO_2@AgO nanocomposite: synthesis, characterization, and investigation of its photocatalytic application. Journal of Electronic Materials *48*, 3285–3296. https://doi.org/10.1007/s11664-019-07091-z.

[88] Rajeswari, R., and Gurumallesh Prabu, H. (2020). Palladium-decorated reduced graphene oxide/zinc oxide nanocomposite for enhanced antimicrobial, antioxidant and cytotoxicity activities. Process Biochemistry *93*, 36-47. https://doi.org/10.1016/j.procbio.2020.03.010.

[89] Shravana Kumar KN, Raghavendra N, Surendra BS, Kantharjau S, and Mylarappa M (2022). Electrochemical, Photocatalytic and Sensor Studies of Clay/MgO Nanoparticles. Applied Surface Science Advance *10*. 100268. https://doi.org/10.1016/j.apsadv.2022.100268.

[90] Karthika, V., AlSalhi, M.S., Devanesan, S., Gopinath, K., Arumugam, A., and Govindarajan, M. (2020). Chitosan overlaid Fe_3O_4/rGO nanocomposite for targeted drug delivery, imaging, and biomedical applications. Science Reports *10*, 18912. https://doi.org/10.1038/s41598-020-76015-3.

[91] Chandruvasan, S., Madival, H., Mylarappa, M., Naik, N.D., Kantharaju, S., and Bharath, S. (2023). Investigation of antioxidant and photo catalysis of natural honey and cow urine-doped CeO_2 nanoparticles fabricated by reflux method. In Engineering, Science, and Sustainability (CRC Press), pp. 31–36. https://doi.org/10.4324/9781003388982-7.

[92] Hosny, M., Eltaweil, A.S., Mostafa, M., El-Badry, Y.A., Hussein, E.E., Omer, A.M., and Fawzy, M. (2022). Facile synthesis of gold nanoparticles for anticancer, antioxidant applications, and photocatalytic degradation of toxic organic pollutants. ACS Omega *7*, 3121–3133. https://doi.org/10.1021/acsomega.1c06714.

[93] Shahid, S., Ejaz, A., Javed, M., Mansoor, S., Iqbal, S., Elkaeed, E.B., Alzhrani, R.M., Alsaab, H.O., Awwad, N.S., and Ibrahium, H.A. (2022). The anti-inflammatory and free radical scavenging activities of bio-inspired nano magnesium oxide. Front. Mater. *9*, 875163. https://doi.org/10.3389/fmats.2022.875163.

[94] Mylarappa, M., Chandruvasan, S., Thippeswamy, B., Shravana Kumara, K.N., and Kantharaju, S. (2023). Clay incorporated ruthenium oxide nanocomposite for electrochemical, sensor, optical, photocatalytic and antioxidant studies. Sustainable Chemistry for the Environment *2*, 100007. https://doi.org/10.1016/j.scenv.2023.100007.

[95] Turin-Moleavin, Fifere, Lungoci, Rosca, Coroaba, Peptanariu, Pasca, Bostanaru, Mares, and Pinteala (2019). *In Vitro* and *In Vivo* antioxidant activity of the new magnetic-cerium oxide nanoconjugates. Nanomaterials *9*, 1565. https://doi.org/10.3390/nano9111565.

[96] Tudose, M., Culita, D.C., Musuc, A.M., Somacescu, S., Ghica, C., Chifiriuc, M.C., and Bleotu, C. (2017). Lipoic acid functionalized SiO_2@Ag nanoparticles, synthesis, characterization and evaluation of biological activity. Materials Science and Engineering: C *79*, 499–506. https://doi.org/10.1016/j.msec.2017.05.083.

[97] Liang, C., Qiu, H., Han, Y., Gu, H., Song, P., Wang, L., Kong, J., Cao, D., and Gu, J. (2019). Superior electromagnetic interference shielding 3D graphene nanoplatelets/reduced graphene oxide foam/epoxy nanocomposites with high thermal conductivity. Journal of Material and Chemistry C *7*, 2725–2733. https://doi.org/10.1039/C8TC05955A.

[98] Chandruvasan, C., Mylarappa, M., Kantharaju, S, and Rekha, S. (2022). Synthesis and Characterization of rGO Doped Nb_2O_5 Nano Composite for Chemical Sensor Studies. ECS Transitions 107, 269–275. https://doi.org/10.1149/10701.0269ecst.

[99] Karthikeyan, S., Selvapandiyan, M., and Sankar, A. (2022). Electrochemical performance of reduced graphene oxide (rGO) decorated lanthanum oxide (La_2O_3) composite nanostructure as asymmetric supercapacitors. Inorganic Chemistry Communications *139*, 109331. https://doi.org/10.1016/j.inoche.2022.109331.

[100] Xiao, Y., Feng, Z., Huang, X., Huang, L., Long, Z., Wang, Q., and Hou, Y. (2014). Synthesis of lanthanum oxide nanosheets by a green carbonation process. Chinese Science Bulletin, *59*, 1864–1867. https://doi.org/10.1007/s11434-014-0233-6.

[101] Zhang, J., Zhang, Z., Jiao, Y., Yang, H., Li, Y., Zhang, J., and Gao, P. (2019). The graphene/lanthanum oxide nanocomposites as electrode materials of supercapacitors. Journal of Power Sources *419*, 99–105. https://doi.org/10.1016/j.jpowsour.2019.02.059.

[102] Dandia, A., Sharma, A., Parewa, V., Kumawat, B., Rathore, K.S., and Sharma, A. (2015). Amidic C-N bond cleavage of isatin: chemoselective synthesis of pyrrolo[2,3,4- *kl*]acridin-1-ones using AgNPs decorated rGO composite as an efficient and recoverable catalyst under microwave irradiation. RSC Advance *5*, 91888-902. https://doi.org/10.1039/C5RA11747J.

[103] Devi, P.S., Chanu, S.N., Laha, S., and Swain, B.P. (2023). Structural, photoluminescence and electrochemical properties of rGO/La_2O_3 nanocomposites for supercapacitor electrode application. Applied Physics A *129*, 446. https://doi.org/10.1007/s00339-023-06734-7.

[104] Lee, J.W., Kim, S.Y., Rhee, D.Y., Park, S., Jung, J.Y., and Park, M.S. (2022). Tailoring the surface of natural graphite with functional metal oxides via facile crystallization for lithium-ion batteries. ACS Applied Materials and Interfaces *14*, 29797–29805. https://doi.org/10.1021/acsami.2c05583.

[105] Luo, Y., Wang, L., Li, Q., Choi, J., Park, G.H., Zheng, Z., Liu, Y., Wang, H., and Lee, H. (2022). Pseudo-capacitive and kinetic enhancement of metal oxides and pillared graphite

composite for stabilizing battery anodes. Science Reports *12*, 12079. https://doi.org/10.1038/s41598-022-15789-0.

[106] Norouzi, P., Garakani, T.M., and Ganjali, M.R. (2012). Using fast Fourier transformation continuous cyclic voltammetry method for new electrodeposition of nano-structured lead dioxide. Electrochimica Acta *77*, 97–103. https://doi.org/10.1016/j.electacta.2012.05.083.

[107] Mei, H., Mei, Y., Zhang, S., Xiao, Z., Xu, B., Zhang, H., Fan, L., Huang, Z., Kang, W., and Sun, D. (2018). Bimetallic-MOF derived accordion-like ternary composite for high-performance supercapacitors. Inorganic Chemistry *57*, 10953–10960. https://doi.org/10.1021/acs.inorgchem.8b01574.

[108] Zhang, L., Chen, L.-Y., Zhao, C., Liu, Y., and Zhang, L.C. (2019). Calculation of oxygen diffusion coefficients in oxide films formed on low-temperature annealed Zr Alloys and their related corrosion behavior. Metals *9*, 850. https://doi.org/10.3390/met9080850.

[109] Nenkova, R., Wu, J., Zhang, Y., and Godjevargova, T. (2013). Influence of different nanozeolite particles on the sensitivity of a glucose biosensor. Analytical Biochemistry *439*, 65–72. https://doi.org/10.1016/j.ab.2013.04.004.

[110] Shetti, N.P., Malode, S.J., Nayak, D.S., Reddy, K.R., Reddy, Ch.V, and Ravindranadh, K. (2019). Silica gel-modified electrode as an electrochemical sensor for the detection of acetaminophen. Microchemical Journal *150*, 104206. https://doi.org/10.1016/j.microc.2019.104206.

[111] Kang, X., Wang, J., Wu, H., Liu, J., Aksay, I.A., and Lin, Y. (2010). A graphene-based electrochemical sensor for sensitive detection of paracetamol. Talanta *81*, 754–759. https://doi.org/10.1016/j.talanta.2010.01.009.

[112] Wu, C., Tang, Y., Wan, C., Liu, H., and Wu, K. (2015). Enhanced-oxidation and highly-sensitive detection of acetaminophen, guanine and adenine using NMP-exfoliated graphene nanosheets-modified electrode. Electrochimica Acta *166*, 285–292. https://doi.org/10.1016/j.electacta.2015.03.088.

[113] Shubha MB, Manjunatha C, Sudeep M, Chandruvasan S, Sumira Malik and Praveen Sekhar, Development of $NiCoO_2$ Nanoparticles based Electrochemical Sensor with Extremely Low Detection for Hazardous 4-Nitrophenol, J. Electrochem. Soc. 170 (2023) 067509. https://doi.org/10.1149/1945-7111/acdf89.